



HAL
open science

Optimization of a simulation code coupling extended source (k^{-2}) and empirical green's functions:

Application to the case of the middle durance fault

Alain Dujardin, Fabrice Hollender, Mathieu Causse, Catherine Berge-Thierry, Bertrand Delouis, Laetitia Foundotos, Gabriele Ameri, Hussein Shible

► To cite this version:

Alain Dujardin, Fabrice Hollender, Mathieu Causse, Catherine Berge-Thierry, Bertrand Delouis, et al.. Optimization of a simulation code coupling extended source (k^{-2}) and empirical green's functions: Application to the case of the middle durance fault. *Pure and Applied Geophysics*, 2020, 177 (5), pp.2255-2279. 10.1007/s00024-019-02309-x . hal-02877411

HAL Id: hal-02877411

<https://hal.science/hal-02877411>

Submitted on 28 Aug 2021

HAL is a multi-disciplinary open access archive for the deposit and dissemination of scientific research documents, whether they are published or not. The documents may come from teaching and research institutions in France or abroad, or from public or private research centers.


L'archive ouverte pluridisciplinaire **HAL**, est destinée au dépôt et à la diffusion de documents scientifiques de niveau recherche, publiés ou non, émanant des établissements d'enseignement et de recherche français ou étrangers, des laboratoires publics ou privés.



Distributed under a Creative Commons Attribution 4.0 International License



Optimization of a Simulation Code Coupling Extended Source (k^{-2}) and Empirical Green's Functions: Application to the Case of the Middle Durance Fault

ALAIN DUJARDIN,^{1,2}  FABRICE HOLLENDER,^{1,2} MATHIEU CAUSSE,² CATHERINE BERGE-THIERRY,³ BERTRAND DELOUIS,⁴ LAETITIA FOUNDOTOS,¹ GABRIELE AMERI,⁵ and HUSSEIN SHIBLE¹

Abstract—We developed a ground-motion simulation code base on extended rupture modeling combined with the use of empirical Green's functions (EGFs), adapted for low-to-moderate seismicity regions (with a limited set of EGFs), and extended its range of applicability to the lowest source-to-site distances. This code is based on a kinematic source description of an extended fault and is designed to allow complex fault geometries and to generate a ground motion variability in agreement with that of the recorded databases. The code is developed to work with a sparse set of EGFs. Each available EGF is therefore used in several positions on the rupture area. To be used in positions different of their original position, we applied to the EGFs some adjustments. In addition to the classical adjustments (i.e. time delay correction, geometrical spreading correction and anelastic attenuation correction), we propose here a radiation pattern adjustment. The effectiveness of it is tested in a numerical application. We showed noticeable improvements at the lowest distances, and some limitations when approaching the nodal planes of the subevents the recording of which were used as EGFs. We took advantage of the development of this code, its ability to work with a sparse set of EGFs, its ability to take into account complex fault geometries and its ability to master the general variability, to perform a ground-motion simulation scenario on the Middle Durance Fault (MDF). We perform simulations for a hard rock site ($V_{S30} = 1800$ m/s) and a sediment site ($V_{S30} = 440$ m/s) of the CEA Nuclear Research Site of Cadarache (France), and compared the computed ground motion with several ground motion prediction equations (GMPEs). The GMPEs slightly underestimate the sediment site but strongly

overestimate the ground motion amplitude on the hard rock site, even when using a specific correction factor which adapts GMPEs predictions from rock site to hard rock site. This general ascertainment confirms the need to continue efforts towards the establishment of consistent GMPEs applicable to hard-rock conditions.

Key words: Empirical Green's functions, K2 extended source simulations, GMPEs, rock site definition, ground motion simulation variability.

1. Introduction

The aim of this study was to develop ground-motion simulation code based on extended rupture modeling adapted for low-to-moderate seismicity regions, and to extend its range of applicability to the lowest source-to-site distances (i.e. typically distances smaller than the geometric extension of the fault, for which the variation of azimuth between the site and the different extremities of the rupture are non-negligible). This code is based on a kinematic source description of an extended fault according to the k^{-2} model (Causse et al. 2009; Dujardin et al. 2016; Del Gaudio et al. 2018), which is combined with the use of empirical Green's functions (EGFs). It is freely available on github: https://github.com/adujard/K2_FMD/.

Following the EGF approach (Hartzell 1978), small magnitude events are used as EGFs to allow implicit consideration of the characteristics of the propagation medium (e.g., anelastic attenuation, geometrical spreading, site properties). The advantage of this approach is the possibility to simulate ground motion in a wide frequency range when purely numerical approaches are limited by partial

Electronic supplementary material The online version of this article (<https://doi.org/10.1007/s00024-019-02309-x>) contains supplementary material, which is available to authorized users.

¹ French Alternative Energies and Atomic Energy Commission (CEA), CEA Cadarache, DEN/DPIE/SA2S, 13108 Saint-Paul-Lez-Durance, France. E-mail: alain.dujardin@live.fr

² Université Grenoble Alpes, ISTerre, CNRS, IRD, IFSTTAR, 38041 Grenoble, France.

³ French Alternative Energies and Atomic Energy Commission (CEA), CEA Saclay, DEN/DANS/DM2S, 91191 Gif-Sur-Yvette Cedex, France.

⁴ Géoazur, Université de Nice Sophia-Antipolis, Observatoire de la Côte d'Azur, CNRS, 250 rue Albert Einstein, 06560 Valbonne, France.

⁵ SEISTER SAS, 40, Avenue de Lascours, Parc d'activités de Napollon, 13400 Aubagne, France.

knowledge of the small-scale heterogeneities of the propagation medium. However, the deployment of this method in low-to-moderate seismicity areas (as for metropolitan France) is often limited by the number of available small-magnitude events that are usable as EGFs (limited, in addition to the quality of the recording, by range of magnitude, position, depth, focal mechanism; see Dujardin et al. 2016, for details).

The simulation code is then essentially developed for applications with a limited and sparse set of EGFs. This involves being able to use an EGF at a location different from its original position. Therefore, the classical adjustments have been implemented to correct for theoretical differences in geometrical spreading, anelastic attenuation, and travel-time differences between the initial position of the EGF and the position at which it is moved to, to satisfy the lack of data. In addition to these classical adjustments, we implemented a radiation pattern correction, which constitute the most important adjustment and the major contribution of this study.

This adjustment is all the more important because the radiation pattern has a major influence on ground-motion variability at short distances (Dujardin et al. 2018). This correction also makes it possible to improve the prediction at the lowest source-to-site distances, where the applicability of ground-motion prediction equations (GMPEs) is limited due to the lack of data at short distances. Indeed, several studies have highlighted that the use of GMPEs outside the magnitude and distance ranges covered by the datasets from which they are derived leads to misestimation of the ground motion (Bommer et al. 2007; Chiou et al. 2010; Douglas and Jousset 2011). Moreover, close to the fault, the ground motion amplitude is affected by the saturation effect (e.g., Yenier and Atkinson 2014). Although its influence is taken into account through most of the GMPE functional forms (see Fukushima et al. 2003; Zhao et al. 2006), it is only an average consideration for a set of different events and different azimuths. This approach is therefore not suitable for specific site prediction, and does not allow the large azimuth variability of the ground motion and the saturation effect to be taken into account (see Dujardin et al. 2018). Furthermore, the radiation pattern correction

allows some complex fault geometries to be taken into account, with variations of strike and dip angles. This is the case for the geometry of the Middle Durance Fault (MDF) (Guyonnet-Benaize et al. 2015), which constitutes our application case here (see Sect. 4).

Finally, this simulation code is developed in the framework of blind ground-motion prediction in low-to-moderate seismicity areas. This means that it is designed for simulation of a hypothetical future event for which the source characteristics (e.g., stress drop, rupture velocity, rupture dimensions) are a priori unknown. Therefore, the input rupture parameters are defined by the probability density functions, the variability of which can be constrained to reproduce the ground-motion variability observed (for the target event characteristics) in strong-motion databases.

The last part of this paper presents an application of the simulation code, to generate a suite of ground-motion time series for potential ruptures on the MDF, which is located in southeastern metropolitan France, using stations located at the CEA Nuclear Research Site of Cadarache (France). The MDF is a complex system of several segments that has a global extension of about 60 km (Volant et al. 2000), and is mainly oriented North-East to South-West. This application was chosen for several reasons. On the one hand, the fault passes close to the CEA (~ 5 km), and on the other hand, this fault has real seismogenic potential that has been expressed in the recent past by several earthquakes (Fig. 1) of magnitude around 5 (Lambert et al. 1998). Predicting reliable ground motion at or close to the Cadarache site associated to the occurrence of hypothetical earthquakes on the MDF constitutes a scientific challenge, and is clearly an issue for the design and assessment of future or existing facilities in the context of nuclear safety (Berge-Thierry et al. 2017a).

2. General Overview of the k^{-2} Code

2.1. Rupture Area Dimensions

This code was developed to perform ground-motion simulations for a hypothetical event. In this

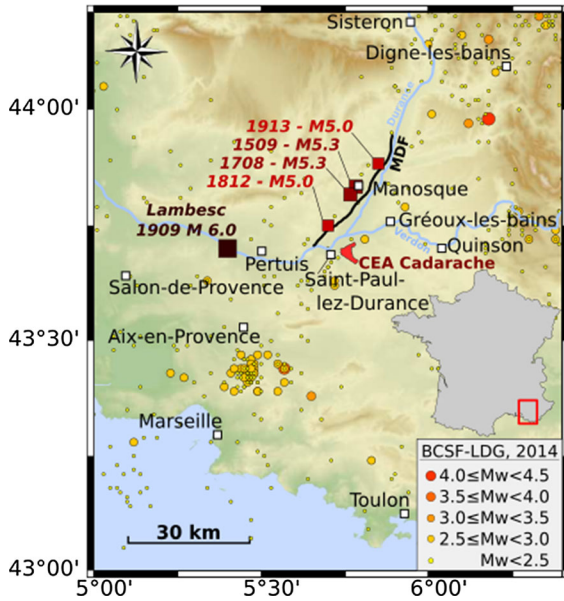


Figure 1

Locations of the Middle Durance Fault (Guyonnet-Benaize et al. 2015), the CEA Cadarache center, and the main historic seismic events (Lambert et al. 1998)

case, there are no available recordings and the physical characteristics of the source are unknown, except for the seismic moment M_0 and the focal mechanism, which are postulated. We first define the size of the fault on which the rupture is expected. Then, the size of the rupture area on this fault, which is assumed to be rectangular, is automatically calculated from the stress drop ($\Delta\sigma$) and the seismic moment M_0 , as originally proposed by Herrero and Bernard (1994).

The stress drop needs to be chosen by the user, for several reasons. First, although the stress drop has been considered as constant since the fundamental work of Aki (1967), it might vary from one region to another (Chouet et al. 1978). Secondly, the variability of the stress drop is significant, with variations generally between 0.1 and 100 MPa (Allmann and Shearer 2009). Moreover, the hypothesis of earthquake self-similarity is questionable, and it is suggested that the constant stress-drop condition is not appropriate for a large range of magnitudes (Mayeda and Walter 1996; Beeler et al. 2003; Kanamori and Rivera 2004; Drouet et al. 2011).

The dimensions of the rupture area are derived as follow: from the input stress drop ($\Delta\sigma$), the

theoretical corner frequency (f_c) is derived following Brune (1970):

$$f_c = \left(\frac{16 \Delta\sigma}{7 M_0} \right)^{1/3} k V_S, \quad (1)$$

where V_S is the S-wave velocity (m/s), M_0 is the seismic moment (Nm), the stress drop is expressed in Pa, and $k = 0.37$ (Brune 1970). Then, according to the following approximation (Hanks 1979; Hanks and McGuire 1981): $f_c = \frac{1}{T_{RUP}}$, where $T_{RUP} = \frac{D_{RUP}}{V_R}$ is the rupture duration and V_R is the rupture velocity (m/s), we derived the length (L) and width (W) of the rupture area by assuming that the characteristic size of the rupture is $D_{RUP} = \sqrt{L^2 + W^2}$. Thus, only the ratio between L and W is necessary to derive the dimensions of the rupture area. V_R depends on V_S in the vicinity of the fault, and it commonly varies between $0.7 * V_S$ and $0.85 * V_S$ (Heaton 1990). V_S in the vicinity of the fault is also used to derive the differences in travel-times between the different parts of the rupture area and the target station. Both V_S and the ratio between V_S and V_R are parameters to be chosen by the user.

2.2. Static Slip Generation

Once the rupture dimensions are defined, the static slip distributions of the source are generated in two steps, as the low and high frequency parts of the static slip are constrained separately. The low frequency part is set to a constant value over the rupture area, as the mean slip, which is derived from the relation between the seismic moment and the rupture dimensions:

$$M_0 = \mu A \bar{D} \quad (2)$$

where $A = L \times W$ is the rupture area, $\mu = \rho V_S^2$ ($\rho = 2.7 \text{ g/cm}^3$), and V_S is the S-wave velocity. The high frequency part of the static slip distributions (representing slip heterogeneities) is defined in the wavenumber domain for any wavenumber $> \sqrt{\left(\frac{1}{L}\right)^2 + \left(\frac{1}{W}\right)^2}$. Following Herrero and Bernard (1994), this high frequency part should have an asymptotic decay in k^{-2} beyond the corner wavenumber k_c . The high frequency part of the displacement spectrum is defined for the rectangular

fault plane similarly to Somerville et al. (1999) and Gallovič and Brokešová (2003):

$$D(k_x, k_y) = \frac{\bar{D}LW}{\sqrt{1 + \left[\left(\frac{k_x}{kc_x} \right)^2 + \left(\frac{k_y}{kc_y} \right)^2 \right]^2}} e^{i\Phi(k_x, k_y)}, \quad (3)$$

where k_x and k_y are the wavenumbers in the strike and the dip directions, respectively, $\Phi(k_x, k_y)$ is the phase spectrum, which is randomly defined, and kc_x and kc_y are the corner wavenumbers in the strike and dip directions. In our code, kc_x and kc_y can be used and interpreted in two ways. First, these corner wavenumbers can be chosen by the user to constrain the characteristic dimensions of slip heterogeneities along the strike and dip ($D_{x,y}^{cara} = \frac{1}{kc_{x,y}}$). This approach therefore makes it possible to control the roughness degree of the static slip (see Causse et al. 2009).

In the second interpretation, the corner wavenumbers associated to the strike and the dip directions are defined as $kc_x = k_C \frac{W}{L}$ and $kc_y = k_C \frac{L}{W}$, in such a way that $\sqrt{kc_x \times kc_y} = k_C$, where k_C is the corner wavenumber. k_C is chosen as the assumed $k_C = \frac{1}{D_{RUP}}$, where $D_{RUP} = T_{RUP} \times V_R$ is the characteristic rupture dimension, and T_{RUP} is the rupture duration, which is proportional to the corner frequency: $f_C = \frac{1}{T_{RUP}}$ (Hanks 1979; Hanks and McGuire 1981). This leads to the following relationship between k_C , the theoretical corner frequency (f_C), and the rupture velocity (V_R):

$$k_C = \frac{f_C}{V_R}. \quad (4)$$

Following this second approach, the corner frequency of the simulated event (with one given moment magnitude, M_0) does not depend on the rupture dimensions (i.e., L , W) nor on the rupture velocity (V_R), but only on the static stress drop chosen as an input parameter. Thus, in this approach, the corner frequency variability is directly controlled by the variability of the input parameter $\Delta\sigma$.

2.3. Spatial Sampling

The rupture area is discretized into subfaults where their sizes are defined according to the target maximum frequency of the simulations. Indeed, the

static displacement amplitude spectrum (Eq. 3) is valid only up to the Nyquist wavenumber (k_{NY}), which depends on the sampling rate in the spatial domain (subfault size SF_{dim}):

$$k_{NY} = \frac{k_{ech}}{2} = \frac{1}{2 \times SF_{dim}}. \quad (5)$$

The generated ground-motion spectra are then limited to the maximum frequency defined by $f_{kmax} \approx k_{NY} \times V_R$. The subfault size SF_{dim} is then automatically defined in the code according to the maximum target frequency (f_{kmax}):

$$SF_{dim} = \frac{V_R}{2 \times f_{kmax}}. \quad (6)$$

Note that our approach differs from the EGF formulation based on scaling laws between large and small earthquakes, in which the subfault size depends on the EGF seismic moment (e.g., Irikura and Kamae 1994; Miyake et al. 2003; Asano 2018). As explained in Sect. 2.5, the EGFs are processed so that they can be treated as approximations of “real” Green’s functions (flat displacement amplitude spectrum and unit seismic moment).

2.4. Rupture Kinematics

The rupture kinematics describes the space–time evolution of slip on the fault plane. First, the rupture time at position (x, y) on the fault is defined as $T_{x,y} = D_{nuc}(x, y)/V_R$, where $D_{nuc}(x, y)$ is the distance to the nucleation point and V_R is the average rupture velocity. Following the approach of Hisada (2000, 2001), we introduce rupture velocity variations through perturbations of the rupture time, distributed over the rupture area, also according to a k^{-2} model. The rupture time is given by:

$$T(x, y) = \frac{D_{nuc}(x, y)}{V_R} \times (1 + \Delta T_R(x, y)), \quad (7)$$

where $\Delta T_R(x, y)$ is the rupture time variation, expressed as a percentage where its maximum controls the roughness level of the propagation front. Following the Hisada (2001) formulation, the amplitude spectrum of the rupture time variations on the rupture area is given by:

$$\Delta T_k(k_x, k_y) = \frac{1}{\sqrt{1 + \left[\left(\frac{k_x}{kc_{Tx}} \right)^2 + \left(\frac{k_y}{kc_{Ty}} \right)^2 \right]^2}}, \quad (8)$$

where kc_{Tx} and kc_{Ty} are the corner wavenumbers in the strike and dip directions, respectively. As for the high frequency slip distribution (Eq. 3), the corner wavenumbers control the characteristic size ($Dim_{\Delta T_R}^{x,y}$) of the time perturbation in the strike and dip directions:

$$Dim_{\Delta T_R}^{(x,y)} = \frac{1}{kc_{T(x,y)}}. \quad (9)$$

Second, the slip rate function is defined as the sum of the isosceles triangles as proposed by Hisada (2001). The slip rate function can be parameterized by three parameters : the slip rate function duration τ_{rise} (defined as τ_{max} in Hisada (2001)), the number of summed triangles (Nv) and Ar which corresponds to the ratio of the area of the $j+1$ th triangle with respect to the ratio of the j th triangle (i.e. $Ar = A_{j+1}/A_j$). In the following of the paper we use $Nv = 4$ and $Ar = \sqrt{2}$ for a M 6.0 event. Hisada (2001) showed that it has two characteristics frequencies: $f_1=1/(2\tau_{rise})$, where τ_{rise} is the rise time (i.e., the slip rate function duration) and $f_{max}=1/\tau_1$, where τ_1 is the duration of the first triangle. τ_{rise} is supposed to be constant over the rupture area, and is defined according to Somerville et al. (1999):

$$\tau_{rise} = 2.03 \times 10^{-9} (M_0)^{1/3}, \quad (10)$$

where M_0 is in dyne.cm.

Finally, we obtain the absolute source time function or moment rate function M_0 in the time and frequency domains by summing up the contributions of each subfault (each fault point):

$$M_0(t) = \mu \int_0^L \int_0^W D(x,y) \cdot [SRF(t) * \delta(t - T(x,y))] dx dy, \quad (11)$$

Or as described in the frequency domain (see Eq. 3 in Hisada (2001)):

$$M_0(f) = \mu \int_0^L \int_0^W D(x,y) \cdot [SRF(f) \cdot e^{i\omega T(x,y)}] dx dy, \quad (12)$$

where x and y denote the along-strike and along-dip directions, respectively. μ is the rigidity, $D(x,y)$ is the static slip (see Sect. 2.2), $T(x,y)$ is the rupture time, and $SRF(t)$ is the normalized slip rate function (that is corresponding to unite slip). Hisada (2001) shown empirically that such a slip rate function associated with the above-mentioned k^{-2} distributions of static slip and rupture time perturbations, results in a the classically observed ω^{-2} decay of the moment rate function. More precisely, the slip velocity models, built by superposing equilateral triangles introduce characteristic frequencies: $f_1=1/(2\tau_{rise})$ and f_{max} is imposed by the minimum duration among the triangles. Then, the amplitude spectra of the absolute source time function fall off ω^{-1} before f_1 and as ω^{-2} between f_1 and f_{max} . Note that an additional characteristic frequency f_{kmax} is introduced by the fault discretization. As explained in Sect. 2.3, the subfault size is chosen to reach the target frequency fixed by the user.

2.5. Time Series Generation and Green's Function Corrections

Following the discrete representation theorem (Aki and Richards 2002), the simulated acceleration $U(\vec{r}, t)$ for a station at position \vec{r} is expressed as:

$$U(\vec{r}, t) = \int_0^L \int_0^W R(x,y;t) \cdot FG_{x,y}(\vec{r}, t) dx dy, \quad (13)$$

where $R(x,y;t)$ represents the contribution to the moment rate function at position (x,y) , and $FG_{x,y}(\vec{r}, t)$ is the Green's function in acceleration associated to the same subfault. As mentioned above, there is no specific EGF associated to each subfault. The Green's function $FG_{x,y}(\vec{r}, t)$ at position (x,y) is then approximated using the closest available EGF, $FG_0(\vec{r}, t)$. First, the EGF is deconvoluted from its source spectrum, so as to be considered a Green's function. This deconvolution is performed in the frequency domain, by preserving the EGF phase spectrum. The amplitude source spectrum $S(m_0, f_c)$ is approximated according to the ω^{-2} model (Brune 1970), which depends only on the moment magnitude m_0 and the corner frequency f_c of the EGF:

$$S(m_0, f_c) = \frac{m_0}{\left[1 + \left(\frac{f}{f_c}\right)^2\right]}. \quad (14)$$

Secondly, we apply several adjustments to this Green's function when it is shifted from its original position. We first apply a time shift to the initial Green's function $FG_0(\vec{r}, t)$, which is equal to the travel-time difference $\Delta t(x, y)$ between its initial and new position to the considered station:

$$FG_{x,y}^{adj,1}(\vec{r}, t) = FG_0(\vec{r}, t) * \delta(t - \Delta t(x, y)), \quad (15)$$

with the travel-time difference $\Delta t(x, y)$ defined as follows:

$$\Delta t(x, y) = \frac{R_{STA(\vec{r})}^{SF_{x,y}} - R_{STA(\vec{r})}^{FG_0}}{V_S}, \quad (16)$$

where $R_{STA(\vec{r})}^{SF_{x,y}}$ is the distance between the subfault at position (x, y) on the rupture area and the station considered, and $R_{STA(\vec{r})}^{FG_0}$ is the distance between the initial Green's function and the station.

The difference in the geometrical spreading (defined as $1/R^\gamma$) is corrected as follows:

$$FG_{x,y}^{adj,2} = FG_{x,y}^{adj,1} \times \left(\frac{R_{STA(\vec{r})}^{FG_0}}{R_{STA(\vec{r})}^{SF_{x,y}}}\right)^\gamma. \quad (17)$$

Anelastic attenuation is also accounted for, with it modeled by the quality factor $Q(f)$. The correction is applied in the frequency domain as follows:

$$FG_{x,y}^{adj,3} = iFFT \left(FFT \left(FG_{x,y}^{adj,2} \right) \cdot \exp \left(\frac{-\pi f \left(R_{STA(\vec{r})}^{SF_{x,y}} - R_{STA(\vec{r})}^{FG_0} \right)}{Q_S f^\alpha \times V_S} \right) \right), \quad (18)$$

where FFT is the fast Fourier transform operation, $iFFT$ is the inverse transformation, and $Q(f) = Q_S f^\alpha$ is the quality factor estimation for the S wave, where f is the frequency.

Finally, we implement a frequency dependent radiation pattern correction, as proposed by Pitarka et al. (2000). We use the Aki and Richards (2002) coefficients, computed for S-waves that propagate in a homogeneous infinite elastic medium in the far-field approximation (see Aki and Richards 2002, Eq. 4.33). The Green's function time series first

needs to be expressed in the local coordinate system $(r \theta \Phi)$, specific for each station, which naturally brings out the radial and transverse components of motion (see Aki and Richards 2002, Fig. 4.4). First, the coordinates are rotated from the ENZ to the $(y_1 y_2 y_3)$ coordinate system which is centered on the fault (Fig. 2). The axes $(y_1 y_2 y_3)$ correspond to the axes $(x_2 x_1 - x_3)$ of the Aki and Richards (2002) coordinate system (see Aki and Richards 2002, Fig. 4.4). We consider that for a strike (Φ_S), a dip (δ), and a rake (λ) of 0, the $y_1 (= x_2)$ direction corresponds to the East, the $y_2 (= x_1)$ direction to the North, and the $y_3 (= -x_3)$ direction to the Z direction (Fig. 2). Then the temporal series of Green's functions expressed in the $(y_1 y_2 y_3)$ coordinate system are given by:

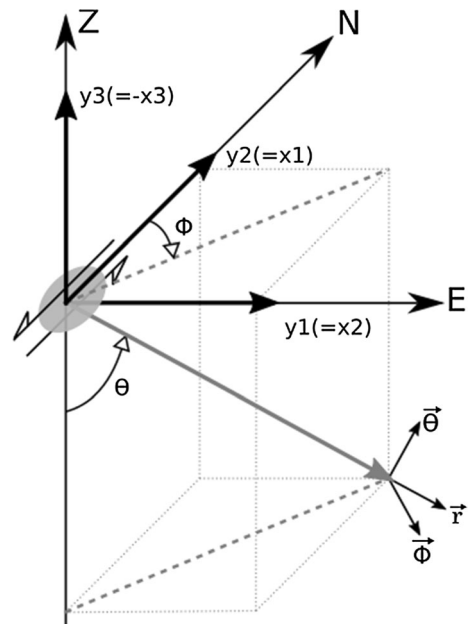


Figure 2

Representation of the $(y_1 y_2 y_3)$ coordinates on the ENZ components orientation. The $(x_1 x_2 x_3)$ coordinates used by Aki and Richards (2002) are also indicated. This case is represented for a strike, a dip, and a rake of zero. The position coordinate θ and Φ used in Eq. (4.33) of Aki and Richards (2002) are also indicated, as are the orientation of the $(r \theta \Phi)$ local coordinate system.

Figure modified from Fig. 4.4 of Aki and Richards (2002)

$$\begin{aligned}
 \begin{pmatrix} FG_{y1} \\ FG_{y2} \\ FG_{y3} \end{pmatrix} &= \underbrace{\begin{pmatrix} \cos(\lambda) & -\sin(\lambda) & 0 \\ \sin(\lambda) & \cos(\lambda) & 0 \\ 0 & 0 & 1 \end{pmatrix}}_{ROT_{\lambda}^{-1}} \\
 \begin{pmatrix} \cos(\delta) & 0 & -\sin(\delta) \\ 0 & 1 & 0 \\ \sin(\delta) & 0 & \cos(\delta) \end{pmatrix} &\begin{pmatrix} \cos(\Phi_S) & -\sin(\Phi_S) & 0 \\ \sin(\Phi_S) & \cos(\Phi_S) & 0 \\ 0 & 0 & 1 \end{pmatrix} \\
 \underbrace{\hspace{1.5cm}}_{ROT_{\delta}^{-1}} &\underbrace{\hspace{1.5cm}}_{ROT_{\Phi_S}^{-1}} \\
 \begin{pmatrix} FG_E \\ FG_N \\ FG_Z \end{pmatrix} &.
 \end{aligned} \tag{19}$$

Note that we also derive the coordinates of the station in the $(y1\ y2\ y3)$ system coordinates by rotating the distance in the North, East and vertical directions between the source and the station:

$$\begin{aligned}
 \begin{pmatrix} STA_{y1} \\ STA_{y2} \\ STA_{y3} \end{pmatrix} &= ROT_{rake}^{-1} \times ROT_{dip}^{-1} \\
 &\times ROT_{strike}^{-1} \begin{pmatrix} STA_E - EGF_E \\ STA_N - EGF_N \\ STA_Z - EGF_Z \end{pmatrix}, \tag{20}
 \end{aligned}$$

where $STA_{E,N,Z}$ and $EGF_{E,N,Z}$ are the positions of the station and the EGF in the ENZ system, respectively, and $STA_{y1,y2,y3}$ is the position of the station in the $(y1\ y2\ y3)$ coordinate system. In this way, it is possible to compute the spherical coordinates θ and Φ of the station position and rotate the Green's function time series into the $(r\ \theta\ \Phi)$ local coordinate system (Fig. 2; see also Aki and Richards 2002, Fig. 4.4):

$$\begin{aligned}
 \begin{pmatrix} FG_{\Phi} \\ FG_r \\ FG_{\theta} \end{pmatrix} &= \underbrace{\begin{pmatrix} \cos(\Phi) & -\sin(\Phi) & 0 \\ \sin(\Phi) & \cos(\Phi) & 0 \\ 0 & 0 & 1 \end{pmatrix}}_{ROT_{\Phi}^{-1}} \\
 \underbrace{\begin{pmatrix} 1 & 0 & 0 \\ 0 & \sin(\theta) & -\cos(\theta) \\ 0 & \cos(\theta) & \sin(\theta) \end{pmatrix}}_{ROT_{\theta}^{-1}} &\begin{pmatrix} FG_{y1} \\ FG_{y2} \\ FG_{y3} \end{pmatrix}.
 \end{aligned} \tag{21}$$

Once the Green's function is expressed in the $(r\ \theta\ \Phi)$ coordinate system, we can compute the far-field coefficients A_{ini}^{FP} and A_{ini}^{FS} of the P waves and S

waves, respectively (see Aki and Richards 2002, Eq. 4.33), associated to the initial position of the EGF. As these are expressed in the $(r\ \theta\ \Phi)$ coordinate system (i.e., with $\hat{r}(1, 0, 0)$, $\hat{\theta}(0, 1, 0)$ and $\hat{\Phi}(0, 0, 1)$), the A^{FP} coefficient has only one non-zero component in the \hat{r} direction. The A^{FS} coefficient has two non-zero components: $A^{SH} = A^{FS} \cdot \hat{\Phi}$ associated to the SH-waves, and $A^{SV} = A^{FS} \cdot \hat{\theta}$ associated to the SV-waves. The coefficients A_{ij}^{FP} and A_{ij}^{FS} are then derived for the subfault position on which the Green's function is moved: $\Phi_{S,ij}$, δ_{ij} , and λ_{ij} for the strike, dip, and rake associated to the subfault (i, j) , and θ_{ij} and Φ_{ij} for the relative position in the $(r\ \theta\ \Phi)$ coordinate system of the station to the (ij) subfault. Once expressed in the $(r\ \theta\ \Phi)$ coordinate system, the temporal series can be corrected. However, due to the isotropic nature of the high-frequency radiation pattern (Liu and Helmberger 1985; Takenaka et al. 2003; Takemura et al. 2009; Sawazaki et al. 2011; Kobayashi et al. 2015), a frequency-dependent correction is considered. This correction is thus defined in the frequency domain, as follows:

$$FG_{r,\theta,\Phi}^{adj} = iFFT(FFT(FG_{r,\theta,\Phi} \cdot RPC_{r,\theta,\Phi})), \tag{22}$$

where FFT and $iFFT$ are the fast Fourier transform and the inverse operation, respectively, the dot is a term to term multiplication, and $RPC_{r,\theta,\Phi}$ is the radiation pattern correction (Fig. 3) that is expressed as:

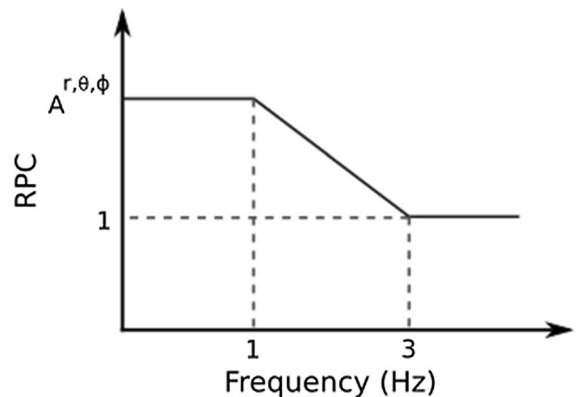


Figure 3
Frequency dependence of the radiation pattern correction (RPC)

$$RPC_{r,\theta,\Phi} = \begin{cases} A^{r,\theta,\Phi} & \text{if } f < 1\text{Hz} \\ \frac{(A^{r,\theta,\Phi}-1)}{(3-1)} \times (f-1) \times A^{r,\theta,\Phi} & \text{if } 1 \leq f < 3\text{Hz} \\ 1 & \text{if } f \geq 3\text{Hz}, \end{cases} \quad (23)$$

where f is the frequency, and $A^{r,\theta,\Phi}$ is the correction coefficient, which is defined as:

$$A^r = \frac{(A_{ij}^{FP} \cdot \hat{r})}{(A_{ini}^{FP} \cdot \hat{r})}; A^\theta = \frac{(A_{ij}^{SV})}{(A_{ini}^{SV})}; A^\Phi = \frac{(A_{ij}^{SH})}{(A_{ini}^{SH})}, \quad (24)$$

Finally, a threshold for this correction is defined. If one of the EGF (i.e. $FG_0(\vec{r}, t)$) radiation pattern amplitudes ($A_{ini}^{FP} \cdot \hat{r}$, A_{ini}^{SH} , A_{ini}^{SV}) is $< 10^{-1}$, no amplitude correction is performed. This limit is intended to avoid having to divide by a number closed to 0, and to avoid strong amplification of the noise when working with real data, which would pollute the simulations.

Then the temporal series are rotated back into the ENZ system coordinates, according to the strike, dip, and rake of the (ij) subfault ($\Phi_{S,ij}$, δ_{ij} and λ_{ij}) and the position of the (ij) subfault relative to the station (θ_{ij} and Φ_{ij}):

$$FG_{ij}^{adj,4} = ROT_{\Phi_{S,ij}} \cdot ROT_{\delta_{ij}} \cdot ROT_{\lambda_{ij}} \left(ROT_{\theta_{ij}} \cdot ROT_{\Phi_{ij}} \left(\begin{pmatrix} FG_{\Phi}^{adj,3} \\ FG_r^{adj,3} \\ FG_{\theta}^{adj,3} \end{pmatrix} \right) \right). \quad (25)$$

A purely numerical test is now carried in Sect. 3. to test the relevance of this correction.

3. Radiation Pattern Correction Test

3.1. Description of the Experiment

To test the efficiency of the radiation pattern correction, the experiment of Dujardin et al. (2018) is reproduced here, in which the impact of the radiation pattern on the saturation effect of the ground-motion peak values is highlighted. According to Dujardin et al. (2018), a M 6.0 event is generated (i.e., $M_0 = 1.1220 \cdot 10^{18}$ Nm). The fault is defined as a plane with a strike of 0° , and a dip of 60° (Fig. 4). The dimensions are fixed for every simulation to $L = 12650$ m and $W = 7900$ m, with fixed input

parameters: $\Delta\sigma = 1.0$ MPa, $f_C = 0.17$ Hz, $V_S = 3600$ m/s, and $V_R = 0.7 \times V_S = 2520$ m/s. The subfault dimensions are fixed to $SF_{dim} = 36$ m, so that the ground-motion simulations are valid up to $f_{kmax} = 35$ Hz (Eq. 6).

A population of 20 static slip distributions is generated using the k^{-2} model (Eq. 3). The rupture times are disturbed according to the model proposed by Hisada (2001) (Eq. 8). The characteristic dimensions of the rupture time variations are fixed between 30% and 70% of the L and W dimensions of the rupture area (Eq. 9). The amplitudes of the rupture time variations are normalized, so as not to exceed 10%, to avoid a propagation front that is too rough, which would generate additional high frequencies beyond what is expected by the ω^{-2} model. The nucleation is located at depth, at distances of $0.15 \cdot L$ along the strike direction, and $0.8 \cdot W$ along the dip direction (Fig. 5). To facilitate the reading of the results, no travel-time correction (Eqs. 15, 16) is considered for any of the cases presented here, to suppress any directivity effects (Dujardin et al. 2018). Simulations are performed for stations located to the North only, at azimuths from -90° to 90° with respect to the fault center, every 22.5° (Fig. 4). The stations are located at rupture distances R_{RUP} of 3, 6, 10, 20, 40 and 70 km.

Three simulation cases are considered. In the first, one unique Green's function is considered, which is located at the center of the rupture area. When this one is shifted from its original position, only the geometrical spreading correction (Eq. 17) and the anelastic attenuation correction (Eq. 18) are considered. In the second case, a single Green's function is also used, but radiation pattern correction (Eqs. 19–25) is added. The third case represents the reference solution, and it allows the effectiveness of this radiation pattern correction to be judged. In this case, the radiation pattern complexity is reproduced by the use of 45 Green's functions distributed every 1.5 km along the strike and dip of the rupture area (Fig. 5).

The Green's functions are computed numerically using the discrete wavenumber method (Bouchon 1981). In every case, these Green's functions are computed for the focal mechanism defined by the strike, dip, and rake angles of 0° , 60° , and 0° ,

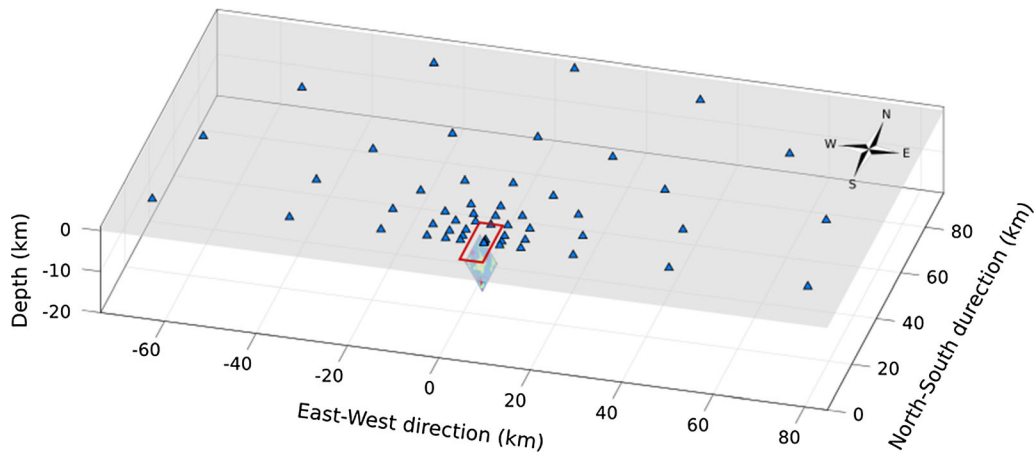


Figure 4

General representation of the experimental geometry. The rupture area is indicated at the center, and its surface projection is shown in red. Stations are represented by blue triangles

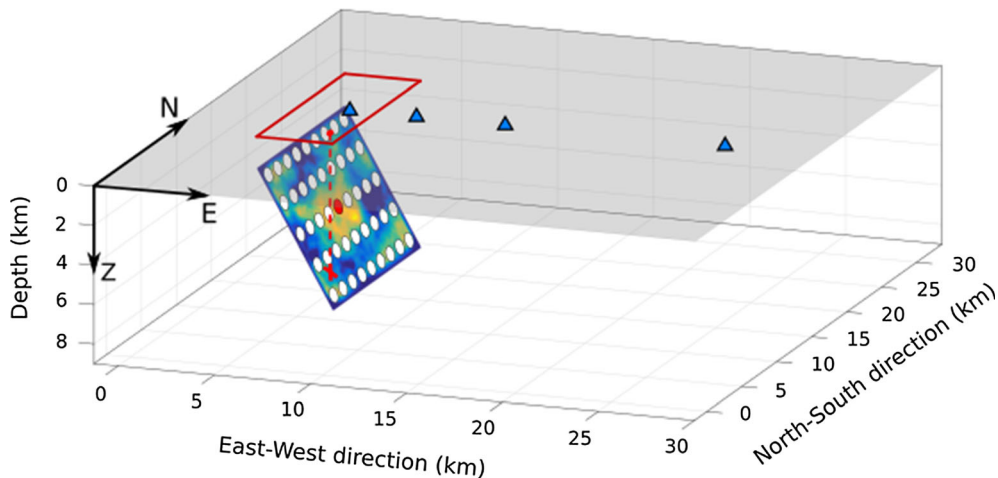


Figure 5

Representation of the fault geometry and its surface projection (red). The four first stations are indicated for the azimuth 90°N . The nucleation position is indicated by the red cross. The positions of the 45 Green's functions used in the third case are indicated in white. The position of the unique Green's function used in the first two cases is indicated in red, at the center of the rupture area

respectively. The propagation medium is assumed to be a homogeneous half space where $V_P = 5000$ m/s and $V_S = 3600$ m/s, and the anelastic attenuation defined through the quality factor is fixed at $Q_P = 50f^{0.2}$ for P waves and $Q_S = 200f^{0.3}$ for S waves. As the propagation medium is homogeneous, the radiation pattern correction is in this case applied to the whole frequency range (Eq. 23).

The results of the three cases are compared in terms of the peak ground acceleration (PGA) versus

the R_{RUP} distance. The PGA for each station is the mean PGA over the 20 rupture realizations. The time series are initially low-pass filtered, at under 35 Hz, then the PGA for each simulation is calculated as the geometric mean of the horizontal components.

3.2. Results

The results show that taking the radiation pattern correction globally improves the results (Fig. 6).

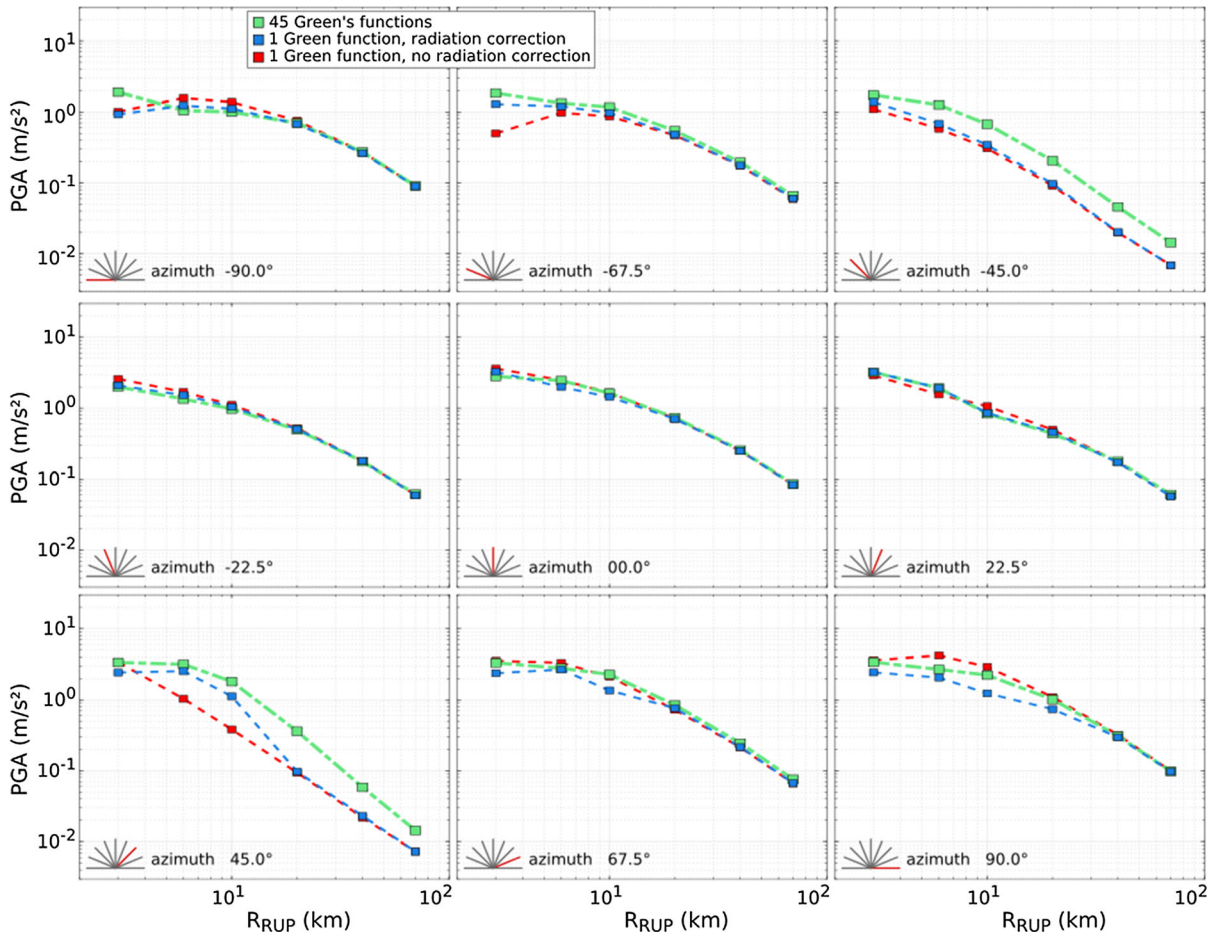


Figure 6

Comparisons of the peak ground acceleration (PGA) of the three simulation cases: one considering a unique Green's function (red), one where this unique Green's function is corrected from the radiation pattern (blue), and the last that uses 45 Green's functions to take into account the radiation pattern complexity (green)

However, there are some limitations in the focal areas of the unique Green's function (azimuths -45° and 45°). At an azimuth of 45° , beyond 20 km the correction is no longer taken into account. This is due to the threshold defined (see Sect. 2.5). Indeed, as this is in a nodal area, the unique Green's function coefficients are weak. For an azimuth of -45° , the value of the radiation pattern is even weaker, due to the east dipping orientation of the fault. The correction is then not applied at any distance (Fig. 6).

4. Application to the Case of the Middle Durance Fault

4.1. Empirical Green's functions

Despite the interest generated by the MDF due to its seismogenic potential (see Fig. 1), the seismicity generated by this fault system is low and hence, there are very few events that can be used as EGFs, and they are often limited by their small magnitudes. However, three events were selected here (Fig. 7). The first event was located approximately in the middle of the fault, almost under the city of Manosque. This event occurred on July 8, 2010, at

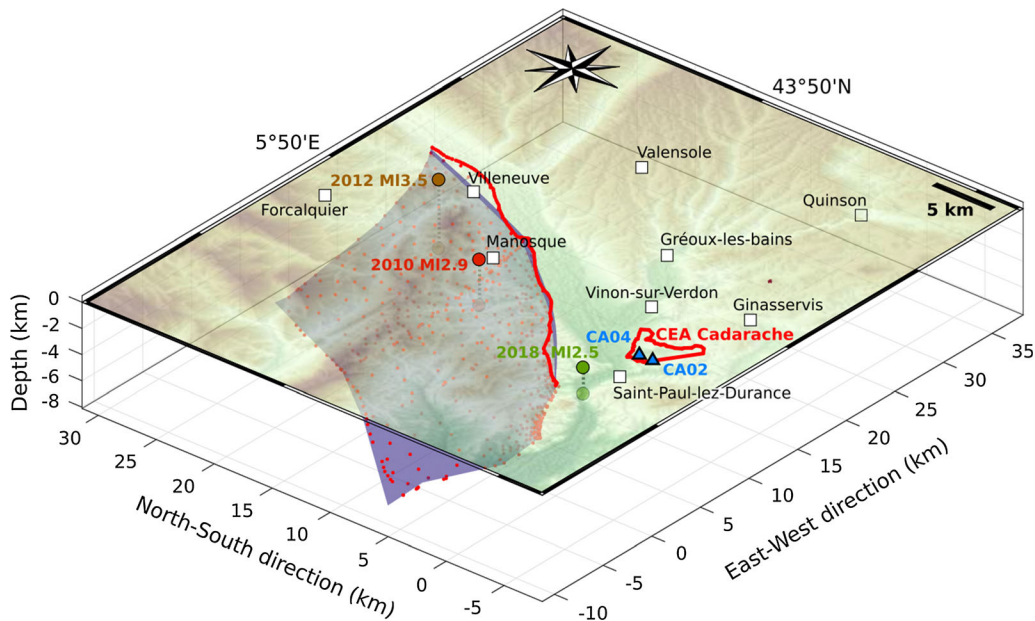


Figure 7

General representation of the application made on MDF. Red dots represent data of the geometry of the fault according to Guyonnet-Benaize et al. (2015). The blue plane represents the present modeling of this geometry. The three EGFs are indicated by the three colored dots, and the stations in the CEA Cadarache center are indicated by blue triangles

20:20, with a magnitude estimated to $M_L = 2.9$. This earthquake was the mainshock of a small seismic sequence that lasted for several weeks. The second event was located on the northern part of the fault, near to the town of Villeneuve, and was recorded on September 19, 2012, at 18:56, with estimated $M_L = 3.5$. This earthquake was also followed by a small seismic sequence that lasted for several weeks. This event was, however, too far from the area of interest, and will therefore not be used. The last event occurred on May 9, 2018, at 06:00, with a magnitude estimated as $M_L = 2.5$. This third event was located on the southern part of the fault, near to the CEA Cadarache site. These empirical Green's functions are of relatively low magnitude, consequently the amplitude of low frequency ground motion is relatively small. Therefore, the computed ground motion was high-pass filtered at 1.1 Hz, which corresponds to the minimum limit below which the signal-to-noise ratio is < 3 (Fig. 8). Note that the EGFs time series have also been visually inspected to ensure the quality of them, including the absence of

unexpected pulse waveform dominating the signal (Fig. S1).

Despite the low-frequency limitation, it was possible to estimate their focal mechanisms (Table 1). The focal mechanism 2010 event was estimated using the *FOCmec* method (Snoke 2003). The focal mechanisms of the 2012 and 2018 events were estimated using the *FMnear* method (Delouis 2014). However, the radiation pattern correction (Eqs. 19–25), which is only applied up to 3 Hz, will have little impact on these simulations, due to the low frequency limit of the EGFs. Two stations on the CEA Cadarache site are common to the three EGFs, thus limiting the simulations at these two sites: the rock site CA02 with $V_{S30} = 1800$ m/s, and the sediment site CA04 with $V_{S30} = 440$ m/s (Perron et al. 2017). These V_{S30} were estimated from in situ measurements involving different approaches: cross-hole measurements, surface-wave-based methods, etc. (Garofalo et al. 2016; Ameri et al. 2017a). These sites are equipped with accelerometers: GeosigAC23 for the 2010 event, and GeosigAC73 for the 2018 event.

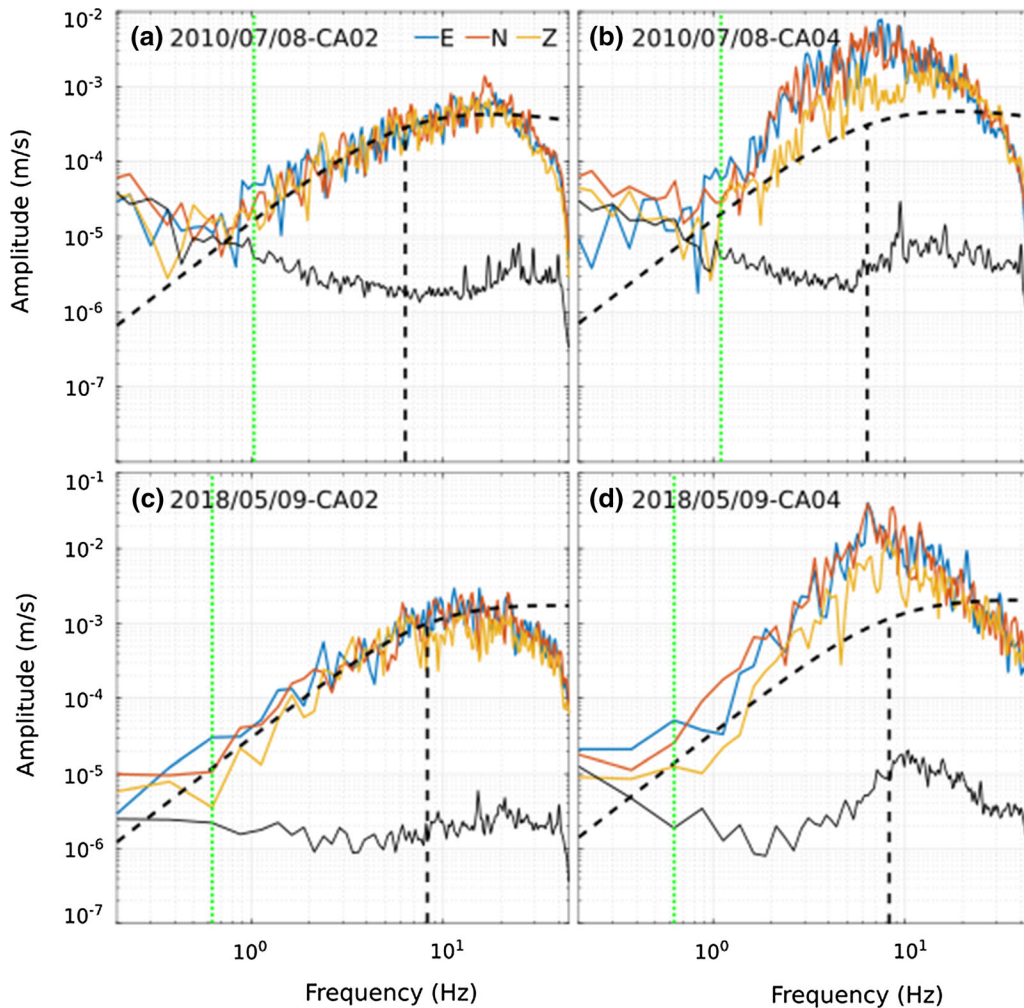


Figure 8

Comparisons of the theoretical ω^{-2} source spectra with the data spectra of the CA02 rock site (a, c) and the CA04 sediment site (b, d). Theoretical ω^{-2} source spectra are computed for M_0 and F_c listed in Table 1. The data spectra are also compared with the noise levels (black curves). The low frequency limit, defined by signal-to-noise ratio < 3 , is shown in green. This low frequency is: 1.0 Hz (a), 1.1 Hz (b), 0.6 Hz (c), and 0.6 Hz (d)

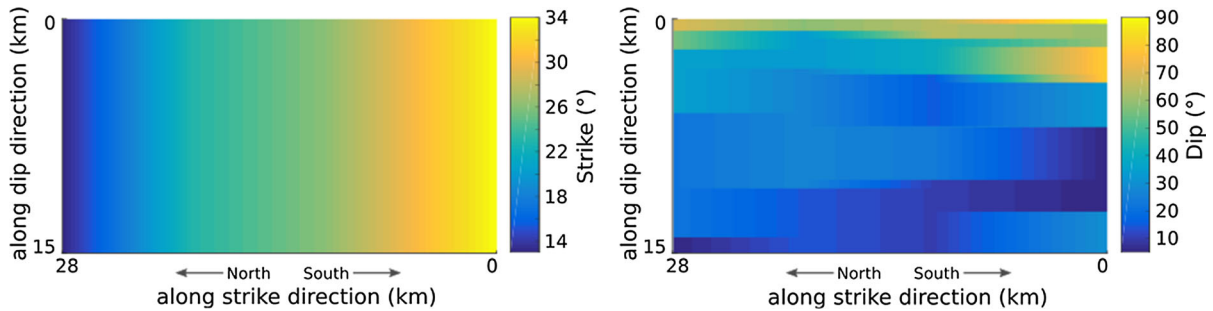
To deconvolute the three EGFs from the influence of their respective sources (Eq. 14), their corner frequencies are also estimated through the Brune (1970) relationship (Eq. 1), using $V_S = 3500$ m/s and $\Delta\sigma = 0.9$ MPa, according to the Drouet et al. (2010) inversion of the French Alps data; see the comparison of a theoretical ω^{-2} source spectrum (Brune 1970) with the data spectra (Fig. 8) on the CA02 rock site station and the CA04 sediment site station (Perron et al. 2017, sites P2 and P3, respectively). All of the EGF metadata used are summarized in Table 1. The

global inversion of the French Alps data realized by Drouet et al. (2010) is intended to determine source terms for each recorded event used, site terms of each station, but also propagation terms such as those describing the geometrical spreading and the anelastic attenuation. Indeed, according to Drouet et al. (2010), $V_S = 3500$ m/s is used for the time correction (Eqs. 15, 16), $\gamma = 1.06$ for the geometrical spreading correction (Eq. 17), and $Q_0 = 336$ and $\alpha = 0.32$ for the anelastic attenuation correction (Eq. 18).

Table 1

List of the three potential EGFs metadata used in the K2 simulation code

Event	Latitude (°N)	Longitude (°E)	Depth (km)	Strike (°)	Dip (°)	Rake (°)	M_L	Mo (Nm)	Fc (Hz)
2010/07/08	43.840	5.781	3.49	186	19	-90	2.9	1.8E13	6.3
2012/09/19	43.895	5.859	2.5	105	45	119	3.5	2.0E14	2.8
2018/05/09	43.700	5.700	2.0	85.0	75.0	147.3	2.5	8.0E12	8.3

Figure 9
Variation of the strike and dip along the MDF

4.2. Geometry of the Fault

The geometry of the fault is built according to Guyonnet-Benaize et al. (2015). The fault is represented as a rectangular area 28 km long by 15 km wide, which is deformed according to the strike and dip variables. The strike progressively varies from 34° to the south, to 13° to the North, and it does not vary with depth (Fig. 9, left). The fault has a listric character toward the West, with strong dip to the East that decreases to the West. However, this is highly variable in the sense that the strike is not constant, and the dip does not vary progressively according to the depth (Fig. 9, right). This fault is then divided into subfaults the dimensions of which are fixed so that the simulations are valid up to a maximum frequency $f_{kmax} = 35$ Hz. Thus, according to Eq. (6), the subfault dimensions are fixed to $SF_{dim} = 35$ m.

4.3. Ground Motion Variability

A M 6.0 magnitude event is generated on the southern part of the fault (i.e., close to the CEA Cadarache center). The variability of the ground motion is assessed through generation of a set of 100 simulations where the source and rupture parameters

vary for each of them (Table 2). The corner wavenumber k_C in Eq. (3) is fixed according to the theoretical corner frequency f_C (Eq. 4), which is therefore directly dependent on the stress drop (Eq. 1). Then, the global ground-motion variability of the simulations is constrained by the stress drop variability. This is constrained according to a log-normal probability distribution (Fig. 10), with a mean of $\Delta\sigma = 0.9$ MPa (Drouet et al. 2010), and a standard deviation of $\tau = 0.2923$, according to Berge-Thierry et al. (2003) that remains comparable to those of more recent GMPEs. The GMPE sigma at 34 Hz (the frequency associated to the PGA) represents the inter-event variability, as it is similar to the intrinsic variability of the data used for regression. The Berge-Thierry et al. (2003) (BT2003) GMPE is considered here, as it is the one that is recommended in the French reference document to assess seismic hazard in the nuclear safety context (Fundamental Safety Rule RFS-2001-01 2001). The results of this study will be compared with this BT2003 GMPE established in 2003 and with more recent ones where the site classifications are more consistent with the shear-wave velocity characteristics of the Cadarache stations studied (see Sect. 4.4).

Table 2

List of the variable parameters for each simulation

No.	$\Delta\sigma$ (MPa)	f_c (Hz)	V_R (m/s)	L (m)	W (m)	D_m (m)	X_{nuc} (m)	Y_{nuc} (m)	Rupture position (%L)	Rupture position (%W)
1	1.3301	0.1805	2530.14	11,935	6440	0.4414	52.0	82.1	3.3	41.9
2	0.9637	0.1622	2832.61	13,300	7175	0.3555	79.7	66.5	1.4	1.6
3	0.9567	0.1618	2807.28	13,335	7210	0.3528	28.1	76.6	1.6	37.5
4	0.8856	0.1577	2693.43	13,685	7385	0.3357	70.7	85.2	1.7	28.4
5	1.0421	0.1664	2930.16	12,950	7000	0.3742	82.4	74.4	1.0	47.4
6	0.8199	0.1536	2856.95	14,035	7595	0.3182	41.7	69.4	0.5	16.9
7	0.8436	0.1551	2821.21	13,895	7490	0.3260	11.7	61.7	0.1	39.8
8	0.6024	0.1386	2454.57	15,540	8400	0.2599	88.2	64.6	21.9	43.7
9	0.7259	0.1475	2866.51	14,595	7910	0.2938	77.0	60.6	0.4	24.3
10	0.6654	0.1433	2896.64	15,050	8120	0.2776	32.1	80.0	19.3	1.1
11	1.0978	0.1694	2708.88	12,740	6860	0.3882	72.1	82.8	1.0	1.1
12	0.7516	0.1493	2695.58	14,455	7805	0.3007	36.0	88.5	4.0	36.4
13	0.9851	0.1633	2786.88	13,195	7140	0.3601	66.5	70.0	2.7	12.8
14	0.9582	0.1618	2554.75	13,335	7210	0.3528	74.8	77.1	1.6	41.0
15	0.7904	0.1518	2608.58	14,210	7665	0.3115	56.2	84.1	21.3	8.9
16	0.7706	0.1505	2686.19	14,315	7735	0.3064	29.2	72.0	5.7	26.1
17	1.3798	0.1828	2639.11	11,795	6370	0.4515	54.4	88.2	2.5	31.1
18	1.2134	0.1751	2622.60	12,320	6650	0.4141	46.1	84.9	4.3	28.6
19	1.3619	0.1820	2674.76	11,830	6405	0.4477	78.3	90.0	0.9	44.4
20	0.9142	0.1593	2472.66	13,545	7315	0.3424	42.5	76.1	1.4	46.9
21	0.6756	0.1440	2917.72	14,980	8085	0.2801	10.5	66.1	1.2	13.7
22	0.7637	0.1501	2511.45	14,350	7770	0.3042	37.4	68.0	5.3	23.8
23	0.7369	0.1483	2921.56	14,525	7840	0.2979	15.3	84.4	13.0	46.2
24	1.2777	0.1781	2587.13	12,110	6545	0.4280	15.9	68.8	7.0	40.0
25	1.5624	0.1905	2774.23	11,305	6125	0.4899	86.8	70.9	8.8	35.0
26	0.9731	0.1627	2612.09	13,265	7175	0.3564	36.8	75.7	1.0	27.7
27	0.8138	0.1533	2517.52	14,070	7595	0.3175	55.5	72.6	0.2	41.2
28	1.1338	0.1712	2563.87	12,600	6790	0.3965	74.4	71.8	4.1	31.4
29	0.5805	0.1369	2969.04	15,750	8505	0.2532	34.5	84.6	21.6	12.8
30	0.8941	0.1582	2884.36	13,615	7350	0.3390	50.6	85.9	1.2	19.9
31	0.6786	0.1443	2923.34	14,945	8085	0.2808	45.6	74.1	7.2	45.3
32	1.0365	0.1661	2507.75	12,985	7000	0.3732	78.8	64.5	3.6	20.4
33	0.7090	0.1464	2713.09	14,735	7945	0.2898	20.5	83.0	6.3	21.7
34	0.7325	0.1480	2523.23	14,560	7875	0.2959	25.2	67.3	1.0	38.0
35	0.9288	0.1602	2471.79	13,475	7280	0.3458	24.5	62.4	1.1	16.2
36	1.4625	0.1863	2752.45	11,585	6265	0.4674	27.3	73.6	6.7	35.7
37	0.9368	0.1606	2782.73	13,405	7245	0.3493	23.9	81.2	2.6	24.5
38	0.8008	0.1524	2731.29	14,140	7630	0.3144	43.5	75.1	0.1	43.2
39	0.5985	0.1383	2944.22	15,575	8400	0.2593	83.5	86.7	13.7	36.2
40	0.8047	0.1527	2835.92	14,105	7630	0.3152	47.9	87.5	0.1	3.0
41	1.0580	0.1673	2864.17	12,880	6965	0.3781	48.8	77.5	1.2	2.5
42	0.9898	0.1636	2951.58	13,160	7105	0.3628	13.7	78.8	1.4	51.0
43	0.8560	0.1559	2718.95	13,825	7455	0.3291	66.7	80.5	0.2	31.4
44	1.1689	0.1729	2591.83	12,460	6720	0.4051	52.0	65.8	5.1	5.9
45	0.9057	0.1588	2461.35	13,580	7315	0.3415	30.6	66.4	2.1	28.8
46	0.8782	0.1572	2828.82	13,720	7420	0.3332	71.5	63.3	1.2	32.7
47	0.8644	0.1564	2850.02	13,790	7455	0.3300	21.8	78.1	0.2	50.1
48	1.3203	0.1801	2680.76	11,970	6475	0.4377	44.8	62.9	0.2	51.5
49	0.7949	0.1521	2810.76	14,175	7665	0.3122	89.8	71.4	7.5	12.4
50	0.6314	0.1408	2945.95	15,295	8260	0.2685	57.3	67.0	12.5	10.5
51	0.9766	0.1629	2652.32	13,230	7140	0.3591	60.1	64.9	2.2	2.5
52	1.5089	0.1883	2801.87	11,445	6195	0.4785	78.0	74.7	7.9	1.6
53	1.7844	0.1991	2498.31	10,815	5845	0.5366	13.3	77.6	10.0	34.8

Table 2 continued

No.	$\Delta\sigma$ (MPa)	f_c (Hz)	V_R (m/s)	L (m)	W (m)	D_m (m)	X_{nuc} (m)	Y_{nuc} (m)	Rupture position (%L)	Rupture position (%W)
54	1.2598	0.1773	2746.27	12,145	6580	0.4245	48.2	89.3	3.1	20.8
55	1.0891	0.1689	2537.68	12,775	6895	0.3851	17.7	76.4	0.5	53.5
56	1.2464	0.1767	2494.68	12,215	6580	0.4221	61.1	60.1	6.8	19.2
57	0.9235	0.1599	2799.39	13,475	7280	0.3458	89.2	69.1	0.2	12.1
58	0.8258	0.1540	2955.00	14,000	7560	0.3205	38.9	71.5	0.2	22.9
59	0.5260	0.1325	2780.67	16,275	8785	0.2373	57.7	87.5	23.1	6.9
60	0.8499	0.1555	2938.61	13,860	7490	0.3268	33.4	69.9	0.4	9.6
61	1.1889	0.1739	2879.26	12,390	6685	0.4096	63.6	80.0	5.2	10.3
62	0.4974	0.1301	2481.77	16,590	8960	0.2282	43.0	68.6	0.9	20.4
63	1.0769	0.1683	2660.77	12,810	6930	0.3821	52.9	65.1	2.7	21.7
64	0.6862	0.1448	2493.15	14,875	8050	0.2833	22.3	79.6	9.5	27.0
65	0.4089	0.1218	2571.92	17,710	9555	0.2005	72.8	81.8	5.6	1.4
66	2.0308	0.2079	2877.03	10,360	5600	0.5847	39.3	71.2	2.1	8.7
67	1.2240	0.1756	2689.63	12,285	6615	0.4174	38.1	87.1	3.7	48.7
68	0.7035	0.1460	2724.06	14,770	7980	0.2878	65.4	80.4	6.6	2.3
69	0.6945	0.1454	2791.73	14,840	8015	0.2852	59.1	65.3	7.4	38.7
70	0.6623	0.1431	2816.63	15,050	8155	0.2764	44.6	67.1	23.2	40.7
71	0.7559	0.1495	2766.86	14,420	7770	0.3028	26.4	60.5	4.7	19.2
72	1.0537	0.1670	2579.74	12,915	6965	0.3771	33.2	82.6	0.5	37.3
73	1.0002	0.1642	2701.59	13,125	7105	0.3638	68.3	88.8	2.3	29.1
74	0.5790	0.1368	2738.45	15,750	8505	0.2532	81.0	81.5	5.1	35.0
75	0.6447	0.1418	2635.17	15,190	8225	0.2715	70.3	84.0	14.3	3.2
76	0.9188	0.1596	2450.20	13,510	7280	0.3449	81.6	73.9	0.7	43.0
77	0.7117	0.1466	2479.78	14,700	7945	0.2905	30.0	61.2	23.0	30.9
78	0.7772	0.1509	2535.54	14,280	7700	0.3085	25.7	61.3	1.2	33.9
79	0.9470	0.1612	2584.28	13,370	7210	0.3519	10.9	81.5	1.5	24.9
80	0.4651	0.1272	2910.74	16,940	9170	0.2184	73.8	67.6	13.1	28.1
81	0.8962	0.1583	2855.84	13,615	7350	0.3390	41.0	63.8	0.7	17.8
82	0.6114	0.1393	2903.69	15,470	8365	0.2621	50.7	88.3	6.9	29.1
83	1.1595	0.1725	2845.60	12,495	6755	0.4019	27.4	85.6	1.6	38.2
84	1.4282	0.1849	2562.06	11,655	6300	0.4620	47.1	72.8	0.5	22.0
85	1.0838	0.1686	2973.19	12,775	6895	0.3851	87.4	70.3	3.1	28.1
86	1.0296	0.1658	2747.89	13,020	7035	0.3704	21.0	63.6	0.9	11.2
87	0.8680	0.1566	2597.15	13,755	7420	0.3324	12.3	72.4	1.0	49.2
88	0.7183	0.1470	2826.01	14,665	7910	0.2924	63.0	86.9	16.2	24.7
89	1.1433	0.1717	2960.75	12,565	6790	0.3976	69.0	77.8	2.8	14.4
90	0.9045	0.1588	2543.88	13,580	7350	0.3399	69.9	61.8	0.4	8.2
91	0.7494	0.1491	2465.33	14,455	7805	0.3007	19.0	82.3	5.1	16.2
92	0.6254	0.1404	2576.40	15,365	8295	0.2662	49.4	86.3	22.2	36.2
93	1.0010	0.1642	2649.14	13,125	7105	0.3638	35.5	74.8	2.2	35.2
94	0.8306	0.1543	2892.44	13,965	7560	0.3213	16.8	77.0	0.5	30.9
95	0.8373	0.1547	2760.99	13,930	7525	0.3236	67.9	78.4	0.2	9.8
96	1.0691	0.1679	2558.54	12,845	6930	0.3811	31.0	65.6	1.1	49.9
97	1.6709	0.1948	2528.74	11,060	5985	0.5125	31.7	75.4	9.3	59.3
98	1.1124	0.1701	2758.11	12,670	6860	0.3903	86.5	68.5	4.0	31.4
99	0.8787	0.1572	2669.44	13,720	7420	0.3332	55.1	62.0	1.1	25.2
100	1.1791	0.1734	2644.17	12,425	6720	0.4063	16.0	87.8	3.3	15.8

X_{nuc} and Y_{nuc} represent the nucleation positions of the rupture expressed as percentages of the length and the width of the rupture area, and calculated from the most southerly point and the closest to the surface point of the rupture area

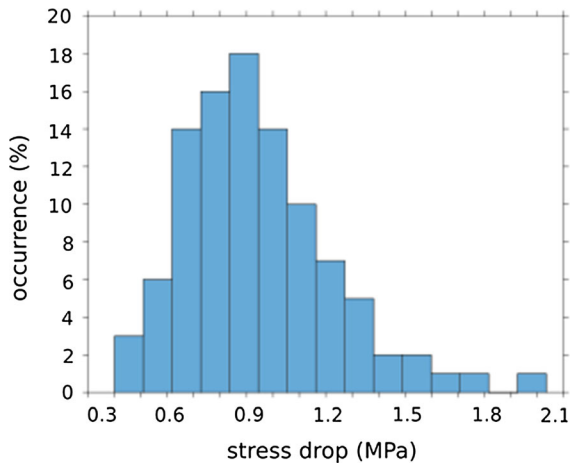


Figure 10

Log-normal distribution of the stress drop for the 100 simulations performed

The stress drop varies between 0.41 MPa and 2.0 MPa (Fig. 10). The rupture velocity V_R commonly varies between $0.7 \cdot V_S$ and $0.85 \cdot V_S$ (Heaton 1990). Then, V_R is defined according to a uniform distribution between these values. For the 100 cases here, a minimum value of V_R of 2450 m/s is obtained, with a maximum value of 2975 m/s.

Following Hisada (2001), rupture-time perturbations are also introduced, defined according to a k^{-2} model (Eq. 8). The characteristic dimensions of the rupture-time variation are randomly fixed between 30% and 70% of L and W (Eq. 9), and the rupture-time variation values are normalized so as not to exceed 10% of the theoretical rupture time (Fig. 11). This value of 10% chosen for the normalization is relatively weak, to avoid the generation of high frequencies in addition to those provided by the k^{-2} model. The nucleation point is randomly defined for each simulation in the deepest half of the rupture area (Figs. 11, 12), so as to be consistent with Mai et al. (2005). The variation of the static slip, the nucleation position and the perturbation of the rupture velocity, make it possible to generate a set of absolute source functions that are highly variable but that nevertheless remain close to the ω^{-2} model of Brune (1970), as intended by the method (Fig. 11). Note however that the ω^{-2} decay is expected only between $f_1 = 1.10$ Hz and $f_{max} = 20.5$ Hz and is supposed to be as ω^{-1} before f_1 .

The rupture dimensions are defined according to the stress drop and the rupture velocity, and in the 100 simulation cases this varies between $L \times W = 10360 \times 5600$ m and $L \times W = 17710 \times 9555$ m (see different examples in Figs. 11 and 12). As the dimensions are derived according to V_R , its variability has no impact on the corner frequency of the simulated event. However, the variation of the dimensions remains a source of variability, as the ground motion amplitude saturation phenomenon depends on it (Yenier and Atkinson 2014).

Finally, the last source of variability comes from the position of the rupture area on the MDF. The rupture area position is defined so as to be on the southern part of the MDF. First, a variation of the rupture area position varies the minimum distance between the rupture area and the station (from 6.3 to 13.5 km for CA02 station, and 5.5–12.7 km for CA04; see Fig. 12). Moreover, the modification of the rupture area position also varies the focal mechanism (i.e., strike and dip) of the simulation event, as the strike and dip vary with the fault geometry (Fig. 12).

4.4. Results

The simulations performed are bandpass filtered between 1.1 Hz and 34 Hz (see synthetic for simulations 8, 12, 36 and 52 in Figure S2). The low-frequency limit is set according to the signal-to-noise ratio of the EGFs (Fig. 8). As the low frequency part is missing in the simulation, i.e., between the corner frequency (~ 0.16 Hz for M 6.0 with $\Delta\sigma = 0.9$ MPa and $V_S = 3500$ m/s according to Eq. 1) and the low-frequency filter limit, we compare the simulated results in terms of the PGA only, with various GMPEs for the horizontal motion (Fig. 13, 14). The peak ground velocity (PGV) is indeed more sensitive to the frequencies around the corner frequency (see Dujardin et al. 2015), and our simulations can therefore not be considered as reliable in terms of the PGV. The PGA of each simulation is calculated as the geometric mean of the horizontal component and represented as a function of the hypocentral, Joyner-Boore and rupture distance (Fig. 13). For comparison, we used several GMPEs. First, we used the Berge-Thierry et al. 2003, (BT2003) since this

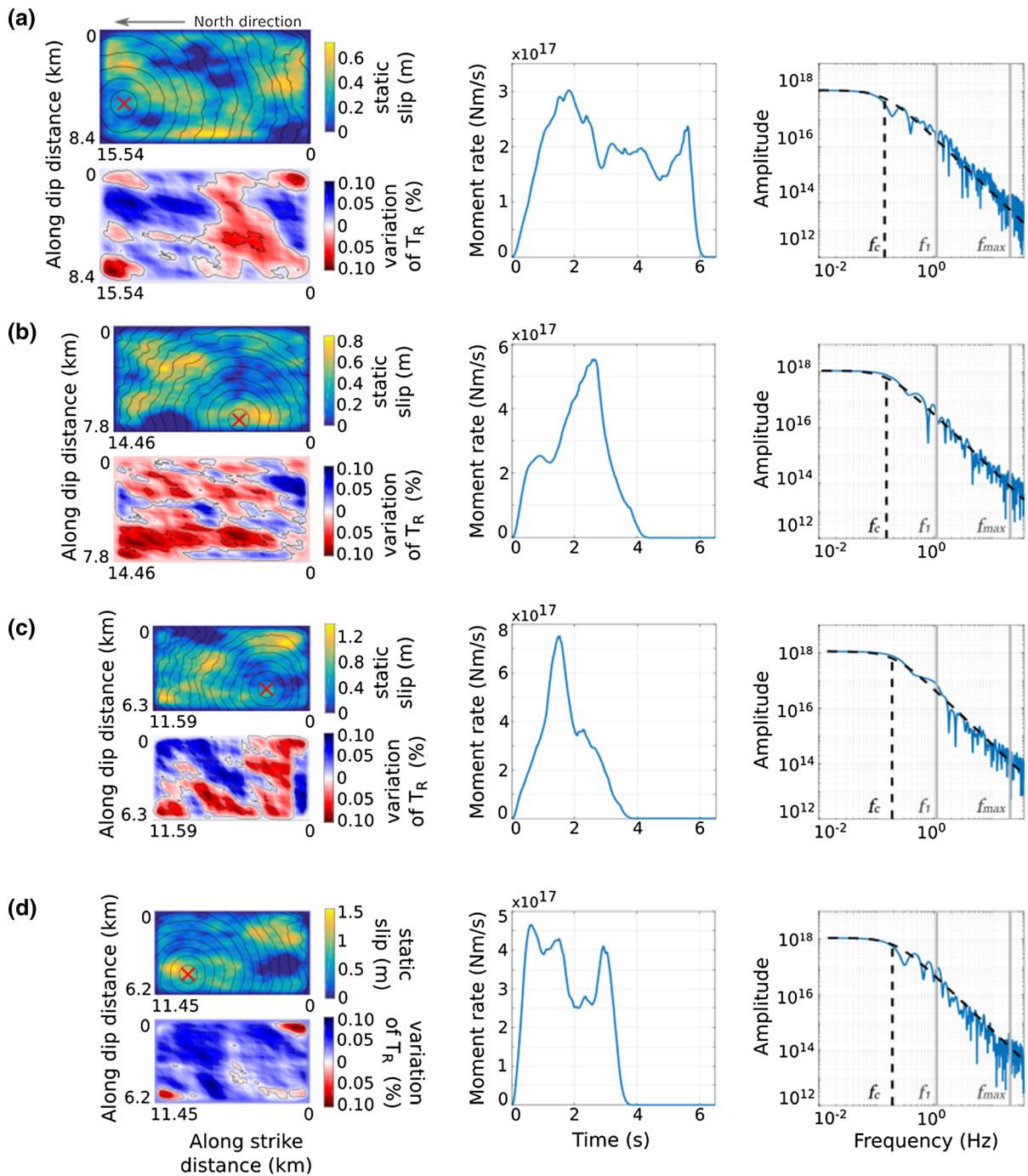


Figure 11

Static slip distribution and T_R variation map (left). The dimensions of the different realizations are scaled. Nucleation points are represented by red crosses. These pairs of maps are used to calculate the absolute source time functions (middle), the spectra of which are compared with the theoretical ω^{-2} spectra computed for the medium value $\Delta\sigma = 0.9$ MPa (right, black dashed lines). The two characteristic frequencies of Hisada $f_1 = 1.10$ Hz and $f_{max} = 20.5$ Hz are represented by gray lines. The cases presented are: simulation 8 (a), simulation 12 (b), simulation 36 (c) and simulation 52 (d)

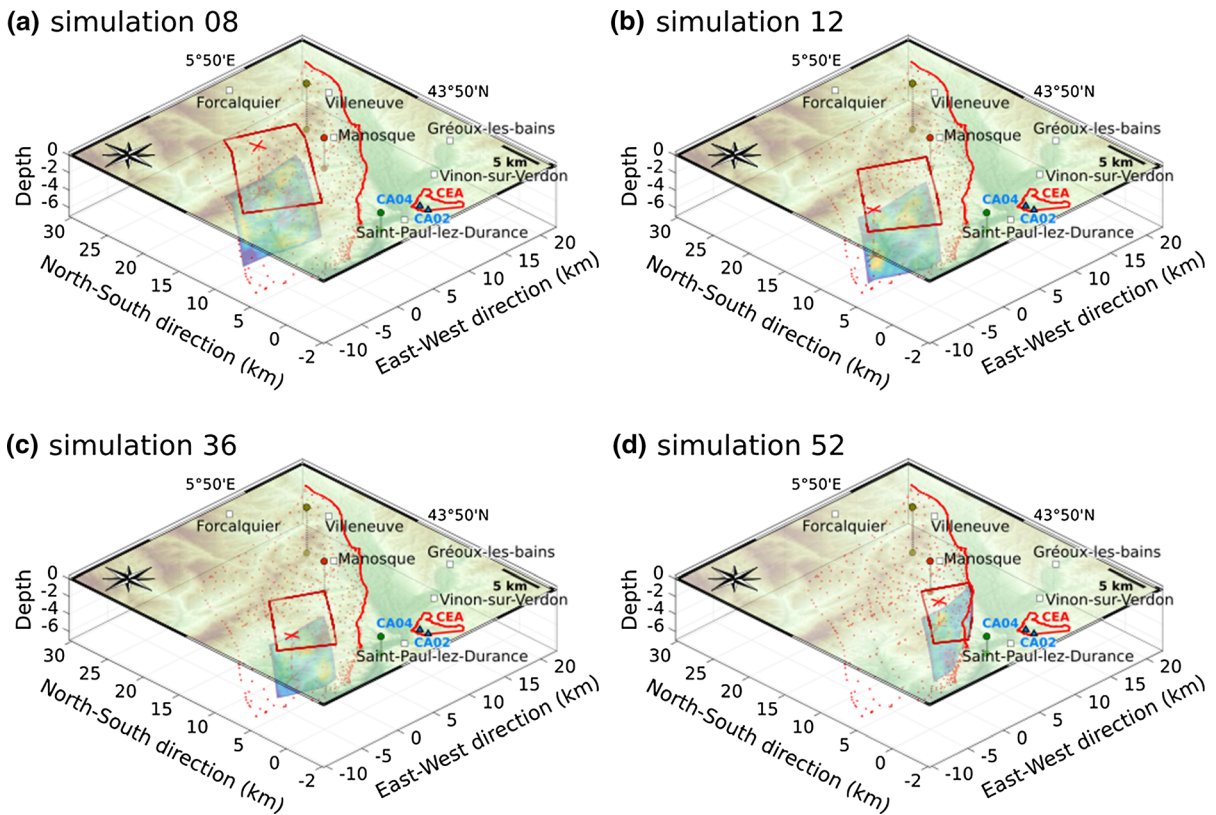


Figure 12

Rupture area positions on the fault of four of the 100 simulations realized. **a** Simulation 08, where the rupture area is one of the largest, with $L \times W$ of $15,540 \times 8400$ m. **b** Simulation 12, with $L \times W$ of $14,455 \times 7805$ m. **c** Simulation 36, with $L \times W$ of $11,585 \times 6265$ m. **d** Simulation 52, which has one of the smallest $L \times W$ of $11,445 \times 6195$ m. The different nucleation positions and their projections to the surface are indicated by the red crosses

GMPE is used within the framework of the French regulation for nuclear facilities. This GMPE has to be used with surface-wave magnitude (M_s). Within the context of Provence seismicity, a specific analysis showed that the Utsu (2002) relationship between M_s and M_w is applicable. In this case, the approximation $M_s \sim M$ is pertinent around magnitude 6. The BT2003 GMPE uses the hypocentral distance (R_{HYP}) metric and can account for two site conditions ('rock' for $V_{S30} > 800$ m/s and 'soil' for $300 \text{ m/s} < V_s < 800$ m/s). In addition to BT2003, we also compare simulation results with the following more recent GMPEs: Ameri et al. (2017b), Akkar et al. (2014), Bindi et al. (2014), Boore et al. (2014), Cauzzi et al. (2015), Campbell and Bozornia (2014), Abrahamson et al. (2014), Chiou and Youngs (2014) and Laurendeau et al. (2017). These GMPEs will be referred

respectively as AM2017, AK2014, BI2014, BO2014, CA2015, CB2014, AB2014, CY2014 and LA2017. All these GMPEs use moment magnitude M_w and will be used here for strike-slip source mechanism. The AM2017, AK2014, BI2014 were derived using a Euro-Mediterranean database. BO2014, CA2015, CB2014, AB2014 and CY2014 were derived using a global database. LA2017 was derived using a subset of the Kiknet database, with a very different approach that will be discussed latter. AK2014, AM2017, BI2014 and BO2014 are computed using the Joyner-Boore distance (R_{JB}). AB2014, CA2015, CB2014, CY2014 and LA2017 are computed using the distance to rupture plan (R_{RUP}). The AM2017 is implemented for 4 EC-8 soil classes, other use the real value of V_{S30} parameter within a given velocity range.

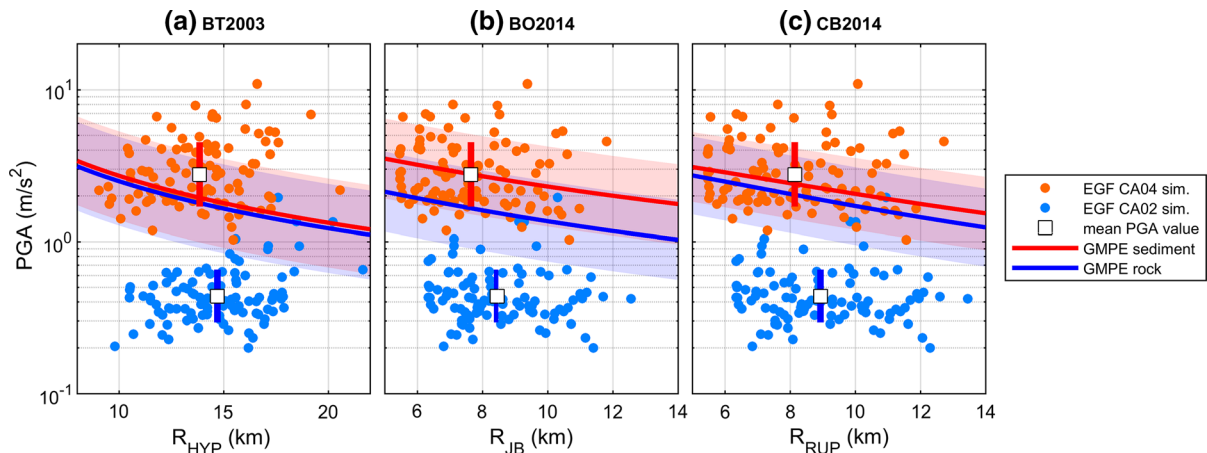


Figure 13

Representation of the peak ground acceleration (PGA) for the 100 simulations for the sites CA02 and CA04. Mean values for each station are shown, with standard deviations at the mean distance of each simulation. The BT2003 (a), BO2014 (b) and CB2014 (c) predictions are added with its standard deviation for the rock and sediment sites. Peaks values are indicated versus the hypocentral distance (a), versus Joyner and Boore distance (b) and versus the rupture distance (c)

Figure 13 shows the results of simulations for stations CA02 (rock site) and CA04 (soil site) for three GMPEs expressed in 3 different metrics: one in R_{HYP} (BT2003, Fig. 13a), one in R_{JB} (BO2014, Fig. 13b) and one in R_{RUP} (CB2014, Fig. 13c).

First, we note strong variability in terms of distance for a given station (e.g., from $R_{HYP} = 9.8$ km to $R_{HYP} = 21.7$ km for the CA02 site, and $R_{HYP} = 9.0$ km to $R_{HYP} = 20.6$ km for the CA04 site; Fig. 13a). Such variability is only possible due to the extended simulation code, which allows variations of the size, the position of the rupture area, and the position of the nucleation. However, despite numerous sources of variability, the ground motion variability is in agreement with that of the GMPEs. This is expected since the simulation variability is constrained according to BT2003 variability. We obtain a mean PGA of 0.4820 m/s^2 for CA02, and 3.1465 m/s^2 for CA04, which defines an amplification factor of 6.5 between CA02 and CA04. This amplification is attributed to the strong high frequency site effects on the CA04 station, with amplifications of up to a factor of 10 between CA02 and CA04 for frequencies above 2 Hz (Perron et al. 2017). This difference is perhaps greater than what would be observed for real data, as these simulations are only based on high frequencies

(> 1.1 Hz), which correspond to the frequency range affected by the site effects. One can note that the non-linear response expected for a large event is usually underestimated when simulations are performed with EGFs, even at rock sites.

We note that the BO2014 is a rather good approximation for the CA04 sediment site (Fig. 13b) with a median very close from the mean of simulated PGA values. For BT2003 and CB2014, EGF simulations shows a mean acceleration few tens of percent higher than the GMPE median (Fig. 13a, c), and the GMPEs largely overestimates the ground motion on the CA02 rock site (Fig. 13). Note that this underestimation may also be due to the use of a sparse set of EGFs which is a limitation of the method in this particular MDF application case.

We test more GMPEs on Fig. 14. Figure 14a (resp. 14b) shows results expressed in R_{JB} (resp. R_{RUP}) for the soil site (CA04). We use the real V_{S30} CA04 values (440 m/s) for all GMPEs to draw corresponding curves, except for the AM2017 for which we use the 'B' EC8-soil class. Figure 14c (resp. 14d) shows same kind of results for the rock site (CA02). Here, we use the upper V_{S30} validity limit of GMPEs to draw curves (1200 m/s for AK2014, BI2014, CA2015; 1500 m/s for BO2014, CB2014, AB2014, CY2014), the 'A' EC8-soil class

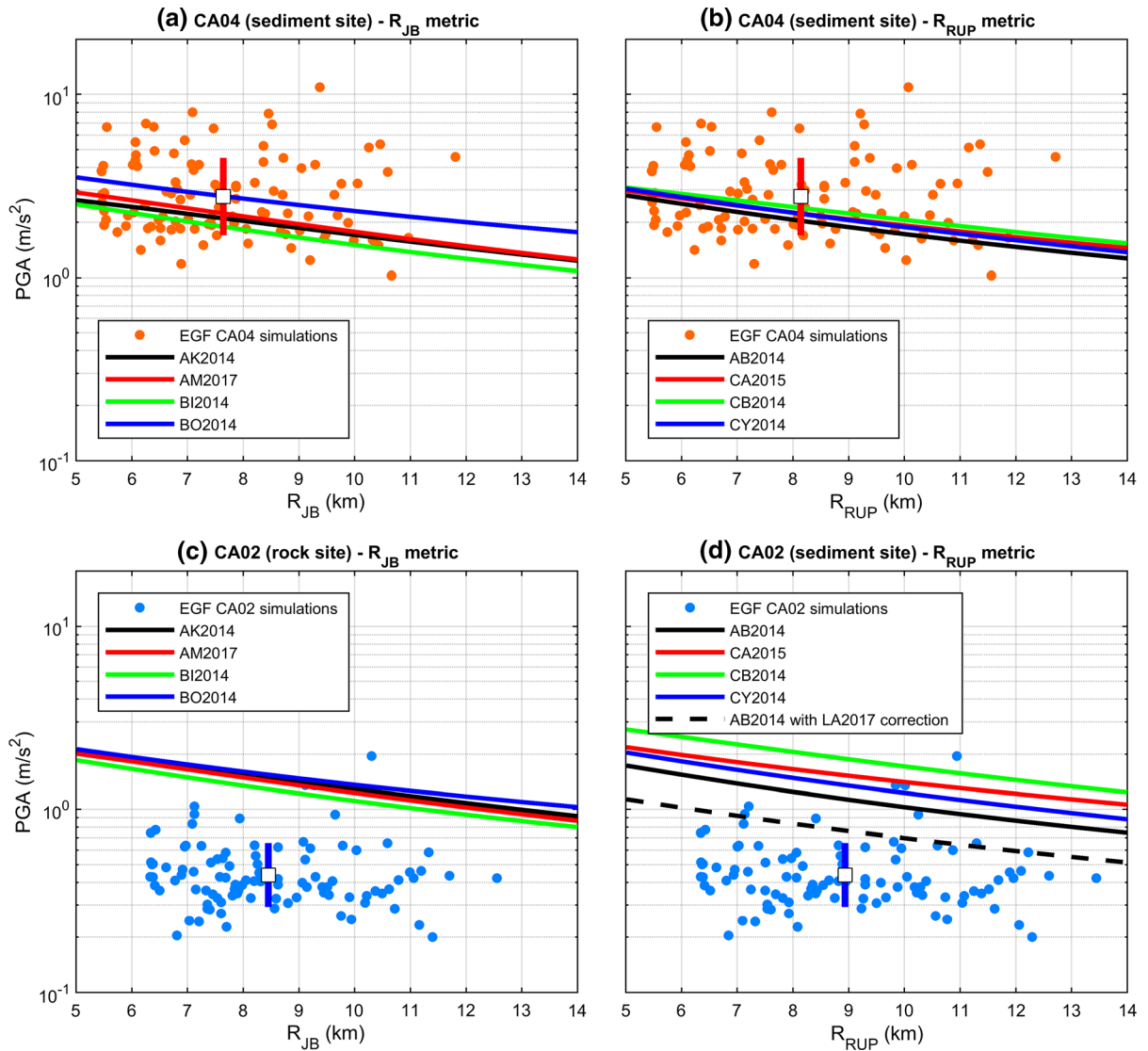


Figure 14

Representation of the PGA for the 100 simulations for the sites CA04 (a, b) and CA02 (c, d). Simulations are compared versus the Joyner–Boore distance with AK2014, AM2017, BI2014 and B02014 GMPEs (a, c), and compared versus the rupture distance with AB2014, CA2015, CB2014, CY2015 and AB2014 with LA2017 correction GMPEs (b, d)

being used for AM2017. On Fig. 14d, we also use the LA2017 as a correction factor applied on another GMPE (here AB2017). Indeed, the LA2017 is derived from a very specific database (Kiknet), it is implemented with quite simple functional form and is built using a quite reduced amount of data. It did not intend to be used ‘as it’, in particular in an European context. However, it integrates a specific site amplification correction applied station by station before its

derivation in order to produce a better estimation for ground motion for hard-rock sites. Here we computed the ratio between the prediction for two site conditions: 440 and 1800 m/s and we apply this correction factor to the AB2014 computed for $V_{S30} = 440$ m/s.

For the soil site (CA04) we see that most of the GMPEs moderately underestimate the simulation of a few tens of percent. This observation remains consistent with the fact that CA04 is affected by high site

amplification (Perron et al. 2017). For the rock site (CA02), on the contrary, all GMPEs strongly overestimate the simulations. The best results (although still significantly overestimating the simulations) are obtained using the LA2017 correction ratio (here applied on AB2014 GMPE). This general ascertainment confirms the need to continue efforts towards the establishment of consistent GMPEs applicable to hard-rock conditions.

5. Discussion and Conclusions

The EGF simulation code presented here was developed for the specific case of low-to-moderate seismicity areas such as metropolitan France, where the main limit is the number of seismic events that can be used as EGFs. To overcome the lack of recorded data for small earthquake, best use is made of the few available EGFs by shifting them from their original positions to sample the whole fault plane, considering some adjustments. In particular, we implemented a radiation pattern correction, the influence of which is preponderant particularly at the shortest distances. This correction was initially tested and validated in a purely numerical case. The results appear promising, with noticeable improvements at the lowest distances, even if we also note some limitations when approaching the nodal planes of the considered EGFs. However, this test was carried out only for a homogeneous medium and deserves to be tested in more realistic media.

We then use this code to simulation of ground motion from M 6.0 scenario earthquakes on the MDF, where the interest in terms of seismic hazard assessment appears obvious. Indeed the MDF is an active fault with a complex geometry. Its geometry has been extensively studied, which has resulted in a well-constrained three-dimensional geological-geophysical model (Guyonnet-Benaize et al. 2015) that can be used to perform full seismic wave propagation simulations. These latter are of huge interest to account for complex phenomena such as nonlinear interactions that can occur between the geological medium and the buildings under strong seismic motions or to perform full physics-based strong-motion predictions for sites or facilities located very

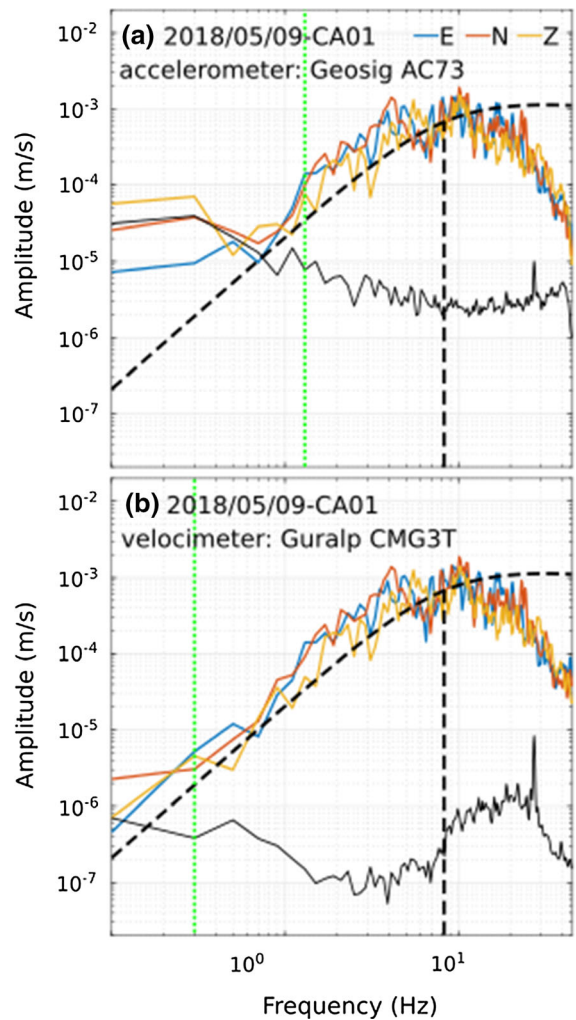


Figure 15

Comparisons of the signal-to-noise ratios for the CA01 site of the CEA Cadarache equipped with both an accelerometer and a velocimeter. The sensors are a Geosig AC473 accelerometer (a), and a Guralp CMG3T velocimeter (b)

close to the MDF system. Such simulations are however limited at high frequency (above ~ 1 Hz).

In the present study, instead of using the three-dimensional velocity model, we took advantage of the available EGFs, which naturally contain information about propagation and site effects over a broad frequency range. During this application, we encountered the classical limitation of the EGF technique at low frequency: due to the small magnitude of the EGF, the signal-to-noise ratio is too small below 1.1 Hz. This limitation had two consequences. First, we did not compute the PGV values, which are

mainly sensitive to frequencies around the corner frequency of the simulated event ($f_c = 0.16$ Hz on average) while our low frequency limit is $f_{min} = 1.1$ Hz. However, this limitation has a negligible impact on the PGA (e.g., Dujardin et al. 2015). Second, the proposed correction of the radiation pattern, which is effective up to 3 Hz only, has a very weak impact on the simulated acceleration.

This raises the question of how to properly model the low frequency ground motion in the framework of EGF simulations. A first solution is the use of EGF recorded by velocimeters rather than accelerometers. We made a comparison for the 2018 event for a site in the CEA Cadarache (CA01 site; which was not used in the present simulations), which is equipped with both an accelerometer (GeosigAC73) and a velocimeter (Guralp CMG3T) (Fig. 15). The velocimeter has a good signal-to-noise ratio from 0.3 Hz (Fig. 15b), while the accelerometer performs well only above 1.3 Hz (Fig. 15a). Another solution is to complement the EGF simulations with low-frequency three-dimensional numerical simulations (in case there is enough information about the propagation medium) or Green's functions using noise correlation (e.g., Denolle et al. 2013, 2014).

Furthermore, the proposed EGF simulation code accounts for complex seismic rupture processes. First, it is possible to incorporate variable strike and dip angles to model complex fault systems as the MDF. Second, the code models complex rupture propagations and generates populations of rupture scenarios with variable rupture dimensions, positions of the rupture area on the fault, slip and rupture time distributions, and nucleation positions. Note that the variability of the simulations can be mastered by constraining the stress drop distribution, which is an input of the code. This makes it possible to generate a ground motion variability in agreement with that of the accelerometric databases, which is an advantage for seismic hazard assessment studies (e.g., for comparisons between site-specific simulations and GMPEs).

Finally, our results are compared with various GMPEs. GMPEs moderately underestimate simulations at the CA04 sediment site ($V_{S30} = 440$ m/s) and strongly overestimate the CA02 hard rock site simulations ($V_{S30} = 1800$ m/s). As mentioned before, the

recording stations of the Cadarache site benefit from direct in situ measurements that enable them to be assigned very well constrained V_{S30} . This is a key information since most of the strong-motion records available in databases worldwide (on which the GMPEs are based and obtained) are not yet associated to a well characterized station, with respect to its specific geological and geophysical properties. These latter properties (e.g., geological stratigraphy, density, P wave and S wave-velocities, depth of main impedance contrasts) are directly responsible for the local seismic site responses.

It is also necessary to point out some important aspects about the use of GMPEs (as detailed in Berge-Thierry et al. 2017a, b, concerning the BT2003 with respect to its use within the framework of the French nuclear regulation). Using generic GMPEs to predict ground motion for a specific site where V_{S30} is far from the class interval boundaries necessarily provides inappropriate results. From this point of view, the results can be anticipated for comparisons between the physics-based ruptures and site-specific predictions of the present study and the GMPEs study. Indeed, with V_{S30} of 440 m/s, CA04 is clearly in the subset of records that are well represented in the motion databases used to derive GMPEs and their associated soil-site coefficients. On the contrary, with its particularly high shear-wave velocities, CA02 is out of the range of the data that are considered to be representative of "hard-rock" responses. An accurate strong-motion prediction for such high V_{S30} is not possible using generic GMPEs (especially if their functional forms do not directly integrate V_{S30} as a proxy). This highlights the need of continuing effort of development of alternative approaches as the one proposed by Laurendeau et al. (2017).

These observations raise several points. First, it raises the question of the ground motion on the hard-rock site, as there is no clear nor consensual definition of the rock, which is particularly problematic as it is needed to get a reference at least to assess the additional specific site effects coming from:

- weathering factors, even on originally healthy rock, that induce lower velocity values within the shallowest layers (first few meters) beneath the surface (see e.g., Hollender et al. 2017). These

effects can induce large amplifications of ground motion at high frequency (e.g. > 10 Hz), even on rock and hard-rock sites;

- impedance contrast or soil properties;
- finally, geometric configurations and fillings for specific substratum.

The GMPEs are indeed based on the use of real databases where characterization of the so-called rock sites is still poorly, if at all, constrained with very few measurements of the V_{S30} proxy and/or the frequency resonance of the site effects. The average prediction is therefore naturally higher than what is expected for a true hard-rock site. Secondly, this result raises the question of taking into account the site effects. Although GMPEs are not suitable for site-specific predictions, the improvement of the functional forms, however, allows at least the one-dimensional site effects to be taken into account. Indeed, some GMPEs consider V_{S30} and/or a site frequency of resonance as a proxy of the functional form. Despite this, more complex effects, such as two-dimensional or three-dimensional resonance basin effects (Causse et al. 2009; Dujardin et al. 2016), or local topographic effects due to short wavelength focusing are still not possible. Consideration of such complex effects must therefore be carried out differently, based, for example, on site-transfer responses.

Finally, the results raise the question of the distance definition used. It appears intuitive to think that R_{RUP} is better suited for the extended fault. This is especially true when distances are small. The results indeed appear to be more consistent when these are represented according to R_{RUP} or alternatively to R_{JB} .

Acknowledgements

This study was carried out under the Sinaps@ project that received French funding managed by the French National Research Agency under the program “Future Investments” (Sinaps@ reference: ANR-11-RSNR-022). Sinaps@ is a “Seism Institute” project (<http://www.institut-seism.fr/en/>, last accessed February 2018).

Open Access This article is distributed under the terms of the Creative Commons Attribution 4.0 International License (<http://creativecommons.org/licenses/by/4.0/>), which permits unrestricted use, distribution, and reproduction in any medium, provided you give appropriate credit to the original author(s) and the source, provide a link to the Creative Commons license, and indicate if changes were made.

Publisher’s Note Springer Nature remains neutral with regard to jurisdictional claims in published maps and institutional affiliations.

REFERENCES

- Abrahamson, N., Silva, W. J., & Kamai, R. (2014). Summary of the ASK14 ground-motion relation for active crustal regions. *Earthquake Spectra*, 30(3), 1025–1055.
- Aki, K. (1967). Scaling law of seismic spectrum. *Journal of Geophysical Research*, 72(4), 1217–1231.
- Aki, K., & Richards, P. G. (2002). *Quantitative seismology*. Sausalito, California: University Science Books. ISBN 0-935702-96-2.
- Akkar, S., Sandikkaya, M. A., & Bommer, J. J. (2014). Empirical ground-motion models for point- and extended-source crustal earthquake scenarios in Europe and the Middle East. *Bulletin of Earthquake Engineering*, 12(1), 359–387.
- Allmann, B. P., & Shearer, P. M. (2009). Global variations of stress drop for moderate-to-large earthquakes. *Journal of Geophysical Research: Solid Earth*, 114(B1), 1.
- Ameri, G., Drouet, S., Traversa, P., Bindi, D., & Cotton, F. (2017a). Toward an empirical ground motion prediction equation for France: Accounting for regional differences in the source stress parameter. *Bulletin of Earthquake Engineering*, 15, 4681–4717. <https://doi.org/10.1007/s10518-017-0171-1>.
- Ameri, G., Hollender, F., Perron, V., & Martin, C. (2017b). Site-specific partially nonergodic PSHA for a hard-rock critical site in southern France: Adjustment of ground motion prediction equations and sensitivity analysis. *Bulletin of Earthquake Engineering*, 15(10), 4089–4111. <https://doi.org/10.1007/s10518-017-0118-6>.
- Asano, K. (2018). Source modeling of an Mw 5.9 earthquake in the Nankai Trough, Southwest Japan, using offshore and onshore strong-motion waveform records. *Bulletin of the Seismological Society of America*, 108, 1231–1239.
- Beeler, N. M., Wong, T. F., & Hickman, S. H. (2003). On the expected relationships among apparent stress, static stress drop, effective shear fracture energy, and efficiency. *Bulletin of the Seismological Society of America*, 93(3), 1381–1389.
- Berge-Thierry, C., Cotton, F., Scotti, O., Griot-Pommer, D. A., & Fukushima, Y. (2003). New empirical response spectral attenuation laws for moderate European earthquakes. *Journal of Earthquake Engineering*, 7(2), 193–222.
- Berge-Thierry, C., Hollender, F., Guyonnet-Benaize, C., Baumont, D., Ameri, G., & Bollinger, L. (2017a). Challenges ahead for nuclear facilities site-specific seismic hazard assessment in

- France: The alternative energies and atomic energy commission (CEA) vision. *Pure and Applied Geophysics*, 174, 9.
- Berge-Thierry, C., Svay, A., Laurendeau, A., Chartier, T., Perron, V., Guyonnet-Benaïze, C., et al. (2017b). Toward an integrated seismic risk assessment for nuclear safety improving current French methodologies through the SINAPS research project. *Nuclear Engineering and Design*, 323, 185–201.
- Bindi, D., Massa, M., Luzi, L., Ameri, G., Pacor, F., Puglia, R., et al. (2014). Pan-European ground-motion prediction equations for the average horizontal component of PGA, PGV, and 5%-damped PSA at spectral periods up to 3.0 s using the RESORCE dataset. *Bulletin of Earthquake Engineering*, 12(1), 391–430.
- Bommer, J. J., Stafford, P. J., Alarcón, J. E., & Akkar, S. (2007). The influence of magnitude range on empirical ground-motion prediction. *Bulletin of the Seismological Society of America*, 97(6), 2152–2170.
- Boore, D. M., Stewart, J. P., Seyhan, E., & Atkinson, G. M. (2014). NGA-West 2 equations for predicting PGA, PGV, and 5%-damped PSA for shallow crustal earthquakes. *Earthquake Spectra*, 30, 1057–1085.
- Bouchon, M. (1981). A simple method to calculate Green's functions for elastic layered media. *Bulletin of the Seismological Society of America*, 71(4), 959–971.
- Brune, J. N. (1970). Tectonic stress and the spectra of seismic shear waves from earthquakes. *Journal of Geophysical Research*, 75(26), 4997–5009.
- Campbell, K. W., & Bozornia, Y. (2014). NGA-West2 ground motion model for the average horizontal components of PGA, PGV, and 5%-damped linear acceleration response spectra. *Earthquake Spectra*, 30(3), 1087–1115.
- Causse, M., Chaljub, E., Cotton, F., Cornou, C., & Bard, P. Y. (2009). New approach for coupling k^{-2} and empirical Green's functions: Application to the blind prediction of broad-band ground motion in the Grenoble basin. *Geophysical Journal International*, 179(3), 1627–1644.
- Cauzzi, C., Faccioli, E., Vanini, M., & Bianchini, A. (2015). Updated predictive equations for broadband (0.01–10 s) horizontal response spectra and peak ground motions, based on a global dataset of digital acceleration records. *Bulletin of Earthquake Engineering*, 13(6), 1587–1612.
- Chiou, B. S. J., & Youngs, R. R. (2014). Update of the Chiou and Youngs NGA ground motion model for average horizontal component of peak ground motion and response spectra. *Earthquake Spectra*, 30(3), 1117–1153.
- Chiou, B., Youngs, R., Abrahamson, N., & Addo, K. (2010). Ground-motion attenuation model for small-to-moderate shallow crustal earthquakes in California and its implications on regionalization of ground-motion prediction models. *Earthquake Spectra*, 26(4), 907–926.
- Chouet, B., Aki, K., & Tsujiura, M. (1978). Regional variation of the scaling law of earthquake source spectra. *Bulletin of the Seismological Society of America*, 68(1), 49–79.
- Del Gaudio, S., Hok, S., Festa, G., Causse, M., & Lancieri, M. (2018). Near-fault broadband ground motion simulations using empirical Green's functions: Application to the Upper Rhine Graben (France–Germany) case study. In *Best Practices in Physics-based Fault Rupture Models for Seismic Hazard Assessment of Nuclear Installations* (pp. 155–177). Birkhäuser, Cham.
- Delouis, B. (2014). FMNEAR: Determination of focal mechanism and first estimate of rupture directivity using near-source records and a linear distribution of point sources. *Bulletin of the Seismological Society of America*, 104(3), 1479–1500.
- Denolle, M. A., Dunham, E. M., Prieto, G. A., & Beroza, G. C. (2013). Ground-motion prediction of realistic earthquake sources using the ambient seismic field. *Journal of Geophysical Research: Solid Earth*, 118(5), 2102–2118.
- Denolle, M. A., Dunham, E. M., Prieto, G. A., & Beroza, G. C. (2014). Strong ground-motion prediction using virtual earthquakes. *Science*, 343(6169), 399–403.
- Douglas, J., & Jousset, P. (2011). Modeling the difference in ground-motion magnitude-scaling in small and large earthquakes. *Seismological Research Letters*, 82(4), 504–508.
- Drouet, S., Bouin, M. P., & Cotton, F. (2011). New moment magnitude scale, evidence of stress drop magnitude scaling and stochastic ground motion model for the French West Indies. *Geophysical Journal International*, 187(3), 1625–1644.
- Drouet, S., Cotton, F., & Guéguen, P. (2010). V_{S30} , κ , regional attenuation and Mw from accelerograms: Application to magnitude 3–5 French earthquakes. *Geophysical Journal International*, 182(2), 880–898.
- Dujardin, A., Causse, M., Berge-Thierry, C., & Hollender, F. (2018). Radiation patterns control the near-source ground-motion saturation effect. *Bulletin of the Seismological Society of America*. <https://doi.org/10.1785/0120180076>.
- Dujardin, A., Causse, M., Courboux, F., & Traversa, P. (2016). Simulation of the basin effects in the Po Plain during the Emilia-Romagna seismic sequence (2012) using empirical Green's functions. *Pure and Applied Geophysics*, 173(6), 1993–2010.
- Dujardin, A., Courboux, F., Causse, M., & Traversa, P. (2015). Influence of source, path, and site effects on the magnitude dependence of ground-motion decay with distance. *Seismological Research Letters*, 87(1), 138–148.
- Fukushima, Y., Berge-Thierry, C., Volant, P., Griot-Pommer, D. A., & Cotton, F. (2003). Attenuation relation for west Eurasia determined with recent near-fault records from California, Japan and Turkey. *Journal of Earthquake Engineering*, 7(4), 573–598.
- Gallovič, F., & Brokešová, J. (2003). On strong ground motion synthesis with k^{-2} slip distributions. *Journal of Seismology*, 8(2), 211–224.
- Garofalo, F., Foti, S., Hollender, F., Bard, P.-Y., Cornou, C., Cox, B. R., et al. (2016). InterPACIFIC project: Comparison of invasive and non-invasive methods for seismic site characterization. Part II: Inter-comparison between surface-wave and borehole methods. *Soil Dynamics Earthquake Engineering*, 82, 241–254. <https://doi.org/10.1016/j.soildyn.2015.12>.
- Guyonnet-Benaïze, C., Lamarche, J., Hollender, F., Viseur, S., Münch, P., & Borgomano, J. (2015). Three-dimensional structural modeling of an active fault zone based on complex outcrop and subsurface data: The Middle Durance Fault Zone inherited from polyphase Meso-Cenozoic tectonics (southeastern France). *Tectonics*, 34(2), 265–289.
- Hanks, T. C. (1979). b values and $\omega - \gamma$ seismic source models: Implications for tectonic stress variations along active crustal fault zones and the estimation of high-frequency strong ground motion. *Journal of Geophysical Research: Solid Earth*, 84(B5), 2235–2242.
- Hanks, T. C., & McGuire, R. K. (1981). The character of high-frequency strong ground motion. *Bulletin of the Seismological Society of America*, 71(6), 2071–2095.
- Hartzell, S. H. (1978). Earthquake aftershocks as Green's functions. *Geophysical Research Letters*, 5(1), 1–4.

- Heaton, T. H. (1990). Evidence for and implications of self-healing pulses of slip in earthquake rupture. *Physics of the Earth and Planetary Interiors*, 64(1), 1–20.
- Herrero, A., & Bernard, P. (1994). A kinematic self-similar rupture process for earthquakes. *Bulletin of the Seismological Society of America*, 84(4), 1216–1228.
- Hisada, Y. (2000). A theoretical omega-square model considering the spatial variation in slip and rupture velocity. *Bulletin of the Seismological Society of America*, 90(2), 387–400.
- Hisada, Y. (2001). A theoretical omega-square model considering spatial variation in slip and rupture velocity. Part 2: Case for a two-dimensional source model. *Bulletin of the Seismological Society of America*, 91(4), 651–666.
- Hollender, F., Cornou, C., Dechamp, A., Oghalaei, K., Renalier, F., Maufroy, E., et al. (2017). Characterization of site conditions (soil class, VS30, velocity profiles) for 33 stations from the French permanent accelerometric network (RAP) using surface-wave methods. *Bulletin of Earthquake Engineering*, 16(6), 2337–2365. <https://doi.org/10.1007/s10518-017-0135-5>.
- Irikura, K., & Kamae, K. (1994). Estimation of strong ground motion in broad-frequency band based on a seismic source scaling model and an empirical Green's function technique. *Annali di Geofisica xxxvii*, 6, 1721–1743.
- Kanamori, H., & Rivera, L. (2004). Static and dynamic scaling relations for earthquakes and their implications for rupture speed and stress drop. *Bulletin of the Seismological Society of America*, 94(1), 314–319.
- Kobayashi, M., Takemura, S., & Yoshimoto, K. (2015). Frequency and distance changes in the apparent P-wave radiation pattern: Effects of seismic wave scattering in the crust inferred from dense seismic observations and numerical simulations. *Geophysical Journal International*, 202(3), 1895–1907.
- Lambert, J., Levret-Albaret, A., Cushing, M., & Durouchoux, C. (1998). *Mille ans de séismes en France, catalogue d'épicentres, paramètres et références* (p. 80). Ouest Editions: Presses Académiques.
- Laurendeau, A., Bard, P.-Y., Hollender, F., Perron, V., Foundotos, L., Ktenidou, O.-J., et al. (2017). Derivation of consistent hard rock ($1000 < v_s < 3000$ m/s) GMPEs from surface and down-hole recordings: Analysis of KiK-net data. *Bulletin of Earthquake Engineering*, 16(6), 2253–2284. <https://doi.org/10.1007/s10518-017-0142-6>.
- Liu, H. L., & Helmlinger, D. V. (1985). The 23:19 aftershock of the 15 October 1979 Imperial Valley earthquake: More evidence for an asperity. *Bulletin of the Seismological Society of America*, 75(3), 689–708.
- Mai, P. M., Spudich, P., & Boatwright, J. (2005). Hypocenter locations in finite-source rupture models. *Bulletin of the Seismological Society of America*, 95(3), 965–980.
- Mayeda, K., & Walter, W. R. (1996). Moment, energy, stress drop, and source spectra of western United States earthquakes from regional coda envelopes. *Journal of Geophysical Research: Solid Earth*, 101(B5), 11195–11208.
- Miyake, H., Iwata, T., & Irikura, K. (2003). Source characterization for broadband ground-motion simulation: Kinematic heterogeneous source model and strong motion generation area. *Bulletin of the Seismological Society of America*, 93(6), 2531–2545.
- Perron, V., Hollender, F., Bard, P. Y., Gélis, C., Guyonnet-Benaize, C., Hernandez, B., et al. (2017). Robustness of kappa (κ) measurement in low-to-moderate seismicity areas: Insight from a site-specific study in Provence, France. *Bulletin of the Seismological Society of America*, 107(5), 2272–2292.
- Pitarka, A., Somerville, P., Fukushima, Y., Uetake, T., & Irikura, K. (2000). Simulation of near-fault strong-ground motion using hybrid Green's functions. *Bull. Seism. Soc. Am.*, 90, 566–586.
- RFS-2001-01 (2001). Règle fondamentale de sûreté n°2001-01 relatives aux installations nucléaires de base. Détermination du risque sismique pour la sûreté des installations nucléaires de base. Nuclear Authority Safety website <https://www.asn.fr/content/download/53897/367951/version/1/.../RFS-2001-01.pdf>.
- Sawazaki, K., Sato, H., & Nishimura, T. (2011). Envelope synthesis of short-period seismograms in 3-D random media for a point shear dislocation source based on the forward scattering approximation: Application to small strike-slip earthquakes in southwestern Japan. *Journal of Geophysical Research: Solid Earth*, 116(B8), 1.
- Snoke, J. A. (2003). FOCMEC: Focal mechanism determinations. *International Handbook of Earthquake and Engineering Seismology*, 85, 1629–1630.
- Somerville, P., Irikura, K., Graves, R., Sawada, S., Wald, D., Abrahamson, N., et al. (1999). Characterizing crustal earthquake slip models for the prediction of strong ground motion. *Seismological Research Letters*, 70(1), 59–80.
- Takemura, S., Furumura, T., & Saito, T. (2009). Distortion of the apparent S-wave radiation pattern in the high-frequency wavefield: Tottori-Ken Seibu, Japan, earthquake of 2000. *Geophysical Journal International*, 178(2), 950–961.
- Takenaka, H., Mamada, Y., & Futamura, H. (2003). Near-source effect on radiation pattern of high-frequency S waves: Strong SH–SV mixing observed from aftershocks of the 1997 North-western Kagoshima, Japan, earthquakes. *Physics of the Earth and Planetary Interiors*, 137(1–4), 31–43.
- Utsu, K. (2002). Relationships between magnitude scales. In W. H. K. Lee, H. Kanamori, P. C. Jennings, & C. Kisslinger (Eds.), *International handbook of earthquake and engineering seismology* (pp. 733–746). Part A: Academic.
- Volant, P., Berge-Thierry, C., Dervin, P., Cushing, M. E., Mohammadioun, G., & Mathieu, F. (2000). The South Eastern Durance Fault permanent network: Preliminary results. *Journal of Seismology*, 4, 175–189.
- Yenier, E., & Atkinson, G. M. (2014). Equivalent point-source modeling of moderate-to-large magnitude earthquakes and associated ground-motion saturation effects. *Bulletin of the Seismological Society of America*, 104(3), 1458–1478.
- Zhao, J. X., Zhang, J., Asano, A., Ohno, Y., Oouchi, T., Takahashi, T., et al. (2006). Attenuation relations of strong ground motion in Japan using site classification based on predominant period. *Bulletin of the Seismological Society of America*, 96(3), 898–913.